

NONTHERMAL EMISSION FROM CLUSTERS OF GALAXIES

DORON KUSHNIR¹ AND ELI WAXMAN¹

Draft version June 23, 2021

ABSTRACT

We show that the spectral and radial distribution of the nonthermal emission of massive, $M \gtrsim 10^{14.5} M_{\odot}$, galaxy clusters may be approximately described by simple analytic expressions, which depend on the cluster thermal X-ray properties and on two model parameters, β_{core} and η_e . β_{core} is the ratio of the cosmic-ray (CR) energy density (within a logarithmic CR energy interval) and the thermal energy density at the cluster core, and $\eta_{e(p)}$ is the fraction of the thermal energy generated in strong collisionless shocks, which is deposited in CR electrons (protons). Using a simple analytic model for the evolution of intra-cluster medium CRs, which are produced by accretion shocks, we find that $\beta_{\text{core}} \simeq \eta_p/200$, nearly independent of cluster mass and with a scatter $\Delta \ln \beta_{\text{core}} \simeq 1$ between clusters of given mass. We show that the hard X-ray (HXR) and γ -ray luminosities produced by inverse Compton scattering of CMB photons by electrons accelerated in accretion shocks (*primary electrons*) exceed the luminosities produced by secondary particles (generated in hadronic interactions within the cluster) by factors $\simeq 500(\eta_e/\eta_p)(T/10\text{keV})^{-1/2}$ and $\simeq 150(\eta_e/\eta_p)(T/10\text{keV})^{-1/2}$ respectively, where T is the cluster temperature. Secondary particle emission may dominate at the radio and very high energy ($\gtrsim 1$ TeV) γ -ray bands. Our model predicts, in contrast with some earlier work, that the HXR and γ -ray emission from clusters of galaxies are extended, since the emission is dominated at these energies by primary (rather than by secondary) electrons. Our predictions are consistent with the observed nonthermal emission of the Coma cluster for $\eta_p \sim \eta_e \sim 0.1$. The implications of our predictions to future HXR observations (e.g. by NuStar, Simbol-X) and to (space/ground based) γ -ray observations (e.g. by Fermi, HESS, MAGIC, VERITAS) are discussed. In particular, we identify the clusters which are the best candidates for detection in γ -rays. Finally, we show that our model's results agree with results of detailed numerical calculations, and that discrepancies between the results of various numerical simulations (and between such results and our model) are due to inaccuracies in the numerical calculations.

Subject headings: acceleration of particles - galaxies: clusters: general - radiation mechanisms: non-thermal - X-rays: general

1. INTRODUCTION

A nonthermal emission component is observed in several clusters of galaxies. In most cases nonthermal radio emission is observed (Feretti 2005), and in some cases a nonthermal hard X-ray (HXR) emission component is also observed (for review, see Rephaeli et al. 2008). The radio emission is interpreted as synchrotron radiation, thereby suggesting that relativistic electrons and magnetic fields are present in the intracluster medium (ICM).

Several models for the synchrotron emission have been presented in the literature. These models differ in the assumptions regarding the origin of the emitting electrons. In some models the emitting electrons are secondary electrons and positrons that were generated by p-p interactions of a cosmic ray (CR) proton population with the ICM (e.g. Dennison 1980; Blasi & Colafrancesco 1999), while in others the high energy of the emitting electrons is achieved by turbulent acceleration of a preexisting ICM population of nonthermal "seed electrons" (secondary or otherwise, e.g. Brunetti et al. 2001; Petrosian 2001; Brunetti & Blasi 2005; Cassano & Brunetti 2005; Cassano et al. 2007; Brunetti et al. 2008). Various sources of CR protons and electrons were considered in the literature, including active galactic nuclei (e.g. Katz 1976; Fabian et al. 1976; Fujita et al. 2007), dark mat-

ter bow shocks (e.g. Bykov et al. 2000), ram-pressure stripping of infalling galaxies (e.g. de Plaa et al. 2006) and shock waves associated with the process of large scale structure (LSS) formation (e.g. Loeb & Waxman 2000; Fujita et al. 2003; Berrington & Dermer 2003; Gabici & Blasi 2003; Brunetti et al. 2004; Inoue et al. 2005). In this paper we consider CRs produced by LSS shocks, and derive predictions for the nonthermal cluster emission they generate. Detailed analysis, based on the predictions of this paper, of the nonthermal radio and HXR emission from a sample of clusters suggests that CR acceleration in LSS shocks is the main source of cluster CRs (Kushnir et al. 2009; Kushnir & Waxman 2010).

The following point regarding the general applicability of our results should be emphasized here. The simple analytic expressions we derive (in § 2) give the non-thermal emission from secondary particles (produced by CR interactions at the cluster core) as a function of β_{core} and of the observed thermal X-ray properties of the cluster. These expressions are valid, for a given value of β_{core} , regardless of the origin of the CRs residing at the cluster core. As shown in (Kushnir et al. 2009), cluster observations already allow one to estimate both the average value of β_{core} and its scatter, $\Delta \ln \beta_{\text{core}}$. The values derived from observations are naturally explained within the frame of the model presented here, where cluster CRs are produced by LSS shocks, and difficult to explain in

¹ Physics Faculty, Weizmann Institute of Science, Rehovot, Israel

other models. Moreover, since alternative models for the origin of cluster CRs must reproduce the observationally inferred values of β_{core} and $\Delta \ln \beta_{\text{core}}$, the non-thermal secondary emission predicted by such models would be similar to that derived here.

There are two primary populations of LSS shocks, which differ in their Mach numbers (see e.g. Ryu et al. 2003; Pfrommer et al. 2006; Skillman et al. 2008): High Mach number shocks generated by the accretion of gas onto filaments and clusters (*accretion shocks*), and low Mach number shocks produced by halo mergers (*merger shocks*). The hypothesis that accretion shocks generate high energy CRs is supported by their resemblance to collisionless non-relativistic shocks in the interstellar medium (see e.g. Keshet et al. 2003), which are generally known to accelerate a power-law distribution of high energy particles (Blandford & Eichler 1987).

Accretion shocks are expected to accelerate electrons to TeV energies. Such electrons, to which we refer as *primary electrons*, lose their energy by inverse Compton (IC) scattering of CMB photons on a time scale which is much shorter than the cluster dynamical time, leading to HXR and γ -ray emission at the vicinity of the shocks (see e.g. Dar & Shaviv 1995; Colafrancesco & Blasi 1998; Loeb & Waxman 2000; Waxman & Loeb 2000; Totani & Kitayama 2000; Kawasaki & Totani 2002). Accretion shocks are also expected to accelerate protons to high energies. The protons, which do not lose their energy on a cluster dynamical time, may be coupled to the thermal plasma by magnetic fields and be confined within the cluster volume over cosmological times. Inelastic collisions of these CR protons with thermal ICM protons would produce high energy γ -rays through the decay of neutral pions, and high energy secondary electrons and positrons through the decay of charged pions (Dennison 1980; Völk et al. 1996; Berezhinsky et al. 1997). The secondary nonthermal emission is dominated by the cluster's core, where the ICM and CR density is highest.

To date, nonthermal emission from accretion shocks has not yet been reliably observed. Furthermore, no cluster of galaxies has so far been firmly detected in γ -rays (Reimer et al. 2003) or in very high energy (VHE, $\gtrsim 1$ TeV) γ -rays (Perkins et al. 2006; Domainko et al. 2007; Perkins 2008) (see, however, the stacking analysis of Scharf & Mukherjee 2002, which revealed a low significance excess of γ -ray emission associated with Abell clusters). As we discuss in § 6, future HXR observations (e.g. NuStar, Simbol-X) and (space/ground based) γ -ray observations (e.g. Fermi, HESS, MAGIC, VERITAS) are expected to provide unambiguous detection of nonthermal emission from accretion shocks.

In order to determine the nonthermal relativistic particle population in clusters, one has to follow the hydrodynamic history of the gas confined within these structures. Nonthermal relativistic particles (CRs) are produced in accretion and merger shocks, and the CR energy density is modified by adiabatic expansion/compression of the gas, and by energy loss due to emission of radiation and due to inelastic nuclear collisions. The CR population in clusters may also be affected by diffusion. Diffusion of CRs on scales ~ 100 kpc would reduce their density at the cores of clusters and hence the secondary emission. The effects of diffusion are difficult to estimate

theoretically, mainly due to our ignorance regarding the structure of magnetic fields within the ICM. However, cluster radio observations imply that diffusion does not significantly affect the secondary population, and that the diffusion time of 100 GeV CRs over scales $\gtrsim 100$ kpc within the ICM is not short compared to the Hubble time (Kushnir et al. 2009). We therefore neglect diffusion in the present analysis.

The evolution of CRs in large-scale structures was investigated numerically in several earlier studies (Keshet et al. 2003; Miniati 2003; Pfrommer et al. 2007, 2008; Pfrommer 2008). All studies identified cluster cores and cluster accretion shocks as the main sources of non-thermal radiation. There are discrepancies between the results of some of the studies, regarding the particles (primaries or secondaries) that dominate the emission at different energies and at different spatial locations. Due to the complicated nature of numerical simulations it is difficult to trace the origin of the discrepancies, which may be largely due to the different values adopted in the simulations for the acceleration efficiencies in shocks. We will resolve here some of these discrepancies by comparing the numerical results with the results of our analytic analysis.

Several earlier studies attempted to provide an analytic derivation of the nonthermal luminosity of galaxy clusters (Sarazin 1999; Fujita & Sarazin 2001; Berrington & Dermer 2003; Gabici & Blasi 2003; Araudo et al. 2008; Murase et al. 2008). These studies did not include a model for the evolution of the space and energy distributions of primary and secondary CRs due to both accretion/merger shocks and adiabatic expansion/compression. Moreover, they did not consider IC emission by primary electrons, which, as we show below, dominates the HXR and γ -ray emission.

We derive in this paper a simple analytic model describing the spatial and spectral distribution of the non-thermal emission produced by cluster CRs. We focus on massive clusters, $M \gtrsim 10^{14.5} M_{\odot}$, since their nonthermal emission is strongest and may be detectable by current and upcoming experiments. We assume that accretion and merger shocks produce power-law momentum distributions of CRs, $d \ln n / d \ln p = -\alpha$, with α determined by the shock Mach number, \mathcal{M} , $\alpha = 4/(1 - \mathcal{M}^{-2}) - 2$ (Blandford & Eichler 1987), and that strong ($\mathcal{M}^2 \gg 1$) shocks deposit a fraction $\eta_{p(e)}$ of the thermal energy they generate in CR protons (electrons). Our description of the accretion shocks, which dominate the CR generation (see § 2), is highly simplified. We assume that the clusters are spherical, that gas is accreted onto clusters in spherically symmetric flows at a rate of $\sim M/t_H$, where t_H is the (instantaneous) Hubble time, and that accretion shocks are strong ($\mathcal{M}^2 \gg 1$). We show (in § 3) that the results of numerical simulations are consistent with an average accretion rate (at low z) of $\approx 0.5M/t_H$.

The nonthermal emission is dominated by primary electrons near the accretion shocks and by secondaries at the cluster core. It is determined therefore mainly by two parameters, η_e and β_{core} , the ratio of the CR energy density (within a logarithmic CR energy interval) and the thermal energy density at the cluster core. We first derive in § 2 simple analytic expressions for the nonthermal emission as function of η_e and β_{core} , and

of the thermal X-ray emission properties of the cluster (the charged secondary, e^\pm , emission, which may dominate at radio wavelengths, depends also on the strength of the ICM magnetic field). We also show, based on simple physical arguments and crude approximations, that $\beta_{\text{core}} \simeq \eta_p/100$ should be expected in massive clusters (see also Pfrommer et al. 2007; Jubelgas et al. 2008). The results of our simple model are shown to be consistent with those of detailed numerical simulations in § 3, with the exception of deviations which are due to inaccuracies of the numerical calculations. In § 4 we compare our model predictions with the observed nonthermal emission of the Coma cluster. The extended HXR emission of Coma is shown to be consistent with our model predictions, and the HXR and radio luminosities are shown to be consistent with our model predictions for $\eta_p \sim \eta_e \sim 0.1$.

Some limitations of our simplified model should be highlighted. Our model does not capture temporal fluctuations in the mass accretion rate and deviations of the accretion flow from spherical symmetry. Since the cooling time of *primary electrons* is short compared to the cluster dynamical time, these effects will lead to temporal fluctuations and to deviations from spherical symmetry of the HXR and gamma-ray emission. Our model approximately describes therefore only the temporally and azimuthally averaged emission of primary electrons. Dedicated numerical simulations that constrain the temporal and spatial fluctuations of the accretion rate will be useful for analyzing upcoming observations (as discussed in detail in § 6). The emission produced by *secondaries*, on the other hand, is not sensitive to the spatial and temporal fluctuations in the accretion of gas. This is due to the fact that the cooling time of CR protons, which produce the secondaries, is long (of the order of the Hubble time). They therefore accumulate in the cluster over its age, and their density at the cluster core, which dominates the secondary emission, is not sensitive to fluctuations in the accretion rate.

In § 5 we examine the validity of the relation $\beta_{\text{core}} \simeq \eta_p/100$. We determine the value of $\beta_{\text{core}}/\eta_p$, its scatter and its dependence on cluster mass using a simple toy model for the evolution of cluster CRs. In order to describe the effects of mergers, we construct (in § 5.1) the merger history of clusters using the scheme of Lacey & Cole (1993), and construct (in § 5.2) a simple model describing the shocks and the adiabatic compression/expansion of the gas induced by mergers, which captures the main features of 3D numerical merger simulations (e.g. McCarthy et al. 2007). Using the simple model of § 5.1 and § 5.2 for the evolution of ICM gas, we construct in § 5.3 a model for the evolution of the CR population. We assume that the effects of diffusion are small, and that CRs are advected with the gas. The evolution of the CR population is followed taking into account energy losses due to Coulomb and inelastic nuclear collisions and assuming that the relativistic particles behave as an ideal gas with an adiabatic index of 4/3 (see e.g. Enßlin et al. 2007). The results of this model slightly modify our crude estimation to $\beta_{\text{core}} \simeq \eta_p/200$, with small scatter and weak dependence on cluster mass.

One limitation of the toy model for ICM evolution is that it includes a description of entropy changes that are driven only by gravity (accretion and merger shocks). It

does not include a description of a possible increase of the entropy at high redshift by non-gravitational processes (such as supernovae, star formation and galactic winds, e.g. Kaiser 1991; Evrard & Henry 1991; Navarro et al. 1995; Cavaliere et al. 1997; Balogh et al. 1999; Ponman et al. 1999), and of the decrease of entropy due to cooling at the centers of massive clusters (see e.g. Fabian 1994; Voigt & Fabian 2004). As explained in § 5.4, for massive clusters, $M \gtrsim 10^{14.5} M_\odot$, these effects are unlikely to modify significantly the main conclusion of § 5.3, $\beta_{\text{core}} \simeq \eta_p/200$, and are therefore unlikely to significantly modify the predicted properties of the nonthermal emission.

In § 6 we explain how our model predictions may be tested, and how the values of the parameters η_p and η_e may be calibrated, using a controlled sample of clusters observed in radio and HXRs. We also discuss our results' implications for future γ -ray observations with space-borne and ground based telescopes. In particular, we identify the clusters which are the best candidates for detection in γ -rays, and the best candidates for detection of emission from pion decays.

Throughout, a Λ CDM cosmological model is assumed with a Hubble constant $H_0 = 70h_{70} \text{ km s}^{-1} \text{ Mpc}^{-1}$, $\Omega_m = 0.23$, $\Omega_b = 0.039$, $\Omega_\Lambda = 1 - \Omega_m$, and $\sigma_8 = 0.9$.

2. A SIMPLE ANALYTIC MODEL FOR THE NONTHERMAL EMISSION

In this section we derive the spectral and radial distribution of the nonthermal emission produced by ICM CRs in massive clusters, $M \gtrsim 10^{14.5} M_\odot$. We assume that the fraction β_{core} of plasma energy carried by CR protons at the central regions of clusters, which dominate the emission from secondary particles, is nearly independent of cluster mass and has a small scatter. We show below that the secondary nonthermal emission of the clusters is determined by their thermal X-ray emission properties and by the value of β_{core} (the secondary e^\pm emission depends also on the strength of the magnetic field within the core). The primary nonthermal emission depends on the thermal X-ray properties and on η_e . This allows us to derive simple analytic expressions for the spectral and spatial distribution of the nonthermal emission. The analytic expressions show explicitly the dependence of the nonthermal emission on model parameters (e.g., the influence of a scatter in β_{core} is easily inferred).

Before going into the details of the model, let us briefly explain, using simple arguments, why we expect $\beta_{\text{core}} \simeq \eta_p/100$ (see also Pfrommer et al. 2007; Jubelgas et al. 2008). As we show in section § 5, the generation of CRs is dominated by accretion shocks. Since accretion shocks are characterized by high Mach numbers, we expect them to produce a flat CR energy spectrum,

$$dn_{\text{CR}}/d\varepsilon \propto \varepsilon^{-2}. \quad (1)$$

For this distribution, the post-shock energy density of CR protons within a logarithmic proton energy interval (around ε) is related to the fraction η_p of the post-shock thermal plasma energy deposited in CR protons by

$$\beta_{\text{CR},p}(\varepsilon) \equiv \frac{\varepsilon^2 dn_{\text{CR},p}/d\varepsilon}{\varepsilon_{\text{gas}}} \approx \frac{\eta_p}{\ln[p_{\text{max}}/(1\text{GeV}/c)]}. \quad (2)$$

Here ε_{gas} is the post-shock thermal plasma energy density and p_{max} is the maximal momentum of the

CR proton spectrum respectively. The maximal momentum is determined by comparing the acceleration time $r_{L,p}c/v_{\text{sh}}^2 \simeq 2.9 \cdot 10^6 \gamma_7 (B_{-7} T_1)^{-1} \text{yr}$ (where $v_{\text{sh}} = 8\sqrt{3T/2m_p}/3$ is the shock velocity, $r_{L,p} = 10^2 \gamma_7 / B_{-7} \text{pc}$ is the Larmor radius of the proton, $\gamma_7 \equiv \gamma/10^7$ is the Lorentz factor of the proton, $B_{-7} \equiv B/0.1 \mu\text{G}$ and $T_1 \equiv T/10 \text{keV}$ is the cluster temperature) to the typical cluster dynamical time, $t_{\text{dyn}} \sim 10^9 \text{yr}$, which gives $p_{\text{max}} \sim 10^{18} \text{eV}/c$. Since $\ln[p_{\text{max}}/(1\text{GeV}/c)] \simeq 20$, $\beta_{\text{CR},p} \simeq \eta_p/20$ right behind the accretion shock.

As we show in section § 5, merger shocks do not significantly affect the CR population. This, and the long (inelastic nuclear collision) cooling time of CR protons,

$$t_{\text{pp}} \simeq (\sigma_{\text{pp}}^{\text{inel}} cn)^{-1} \simeq 2.6 \cdot 10^{10} \left(\frac{n}{10^{-3} \text{cm}^{-3}} \right)^{-1} \text{yr}, \quad (3)$$

where $\sigma_{\text{pp}}^{\text{inel}} \simeq 40 \text{mb}$ and n is the gas number density, implies that the energy density of CR protons produced by the accretion shock is later affected mainly by adiabatic expansion and compression. The difference between the adiabatic indices of the relativistic CRs (4/3) and non-relativistic thermal plasma (5/3) implies $\beta_{\text{CR},p} \propto \rho_{\text{gas}}^{-1/3}$, where ρ_{gas} is the gas density. The ratio between the mean gas density in the core and the gas density behind the accretion shock is typically $\sim 10^2$, implying that the value of $\beta_{\text{CR},p}$ at the cluster core is typically expected to be $\beta_{\text{core}} \simeq \eta_p/100$.

We have ignored in the preceding discussion the fact that different mass elements were accreted at different redshifts, hence at a different densities, which implies that their density compression factor is not given directly by the ratio of densities at the cluster core and at the accretion shock. Moreover, major cluster mergers mix the gas and heat it with weak shocks, such that some deviations from the proposed simple relation are expected. We present in § 5 a simple toy model for the evolution of cluster CRs, which examines the significance of these effects. The model yields $\beta_{\text{core}} \simeq \eta_p/200$, nearly independent of cluster mass and with small scatter among clusters of given mass. We also discuss in § 5 the effects of entropy increase at high redshift (by non-gravitational processes) and of entropy decrease due to cooling at the centers of massive clusters. We argue that these effects are unlikely to modify significantly the predicted properties of the nonthermal emission from massive clusters.

We derive below analytic expressions for the luminosity and surface brightness produced by different emission mechanisms. For convenience, the details of the calculations are given in § A, and only the main results are given in § 2.2–§ 2.5. We note that since the emission from hadronic processes is concentrated at the cluster core, while the emission from primary electrons originates from a thin layer around the accretion shock, the surface brightness profiles produced by primary and secondary particles are different. One may therefore distinguish between the two sources of nonthermal radiation by examining the radial dependence of the nonthermal emission surface brightness. We first describe in § 2.1 the thermal emission properties of galaxy clusters, based on which the nonthermal emission properties are later derived. In § 2.2 and § 2.3 we summarize our model results for the emission from neutral (π^0) and charged (e^\pm) products of inelastic nuclear collisions of CR pro-

tons. In § 2.4 we summarize our model results for the (IC and synchrotron) emission from primary CR electrons. Motivated by the results of Kushnir et al. (2009), who constrain β_{core} based on radio emission, and by the results of Kushnir & Waxman (2010), who constrain η_e based on HXR observations, numerical results are given using a normalization of $\beta_{\text{core}} = 10^{-4}$ and $\eta_e = 0.01$.

The analytic results of § 2.2–§ 2.4 are obtained by using simple approximations for the spectrum of secondaries produced and for the IC and synchrotron spectra (the details are given in § A). In § 2.5 we compare the results of § 2.2–§ 2.4 to those obtained using a more accurate parametrization of the spectrum of p-p secondaries (following Kamae et al. 2006), and using the exact formulae for IC and synchrotron emission (following Blumenthal & Gould 1970). We find that the deviations are small.

The charged secondary emission depends on the the strength of the magnetic field in the cluster core. It is given in § 2.3 in terms of B/B_{CMB} , the ratio of the magnetic field to B_{CMB} , defined as the magnetic field for which the magnetic energy density equals the CMB energy density,

$$B_{\text{CMB}} \equiv (8\pi a T_{\text{CMB}}^4)^{1/2} = 3.2(1+z)^2 \mu\text{G}. \quad (4)$$

Since the secondary e^\pm emission is dominated at high energy, $\gtrsim 1 \text{eV}$, by secondary π^0 decay and by IC emission of primary electrons, the uncertainty in the value of B affects only the predicted radio emission, which is not the main focus of the current paper. The detailed discussion of radio emission from clusters given in Kushnir et al. (2009) indicates that B is within the range of $\sim 1 \mu\text{G}$ to $\sim 10 \mu\text{G}$.

2.1. Clusters of galaxies: thermal emission properties

The thermal X-ray emission of clusters is usually characterized by 4 parameters: L_X , the bolometric luminosity integrated out to some radius r_X from the cluster center; T , the cluster temperature (weighted averaged over the cluster emission); β and r_c , which define the radial surface brightness profile, and hence the radial density profile (Cavaliere & Fusco-Femiano 1976; Gorenstein et al. 1978; Jones & Forman 1984),

$$\rho_{\text{gas}}(r) = \rho_0 \left(1 + \frac{r^2}{r_c^2} \right)^{-(3/2)\beta}. \quad (5)$$

Using the HIFLUCGCS sample of the X-ray-brightest galaxy clusters of Reiprich & Bohringer (2002), which is based on the ROSAT All-Sky X-Ray Survey, we derive the following correlations:

$$\begin{aligned} L_X &= L_{X0} h_{70}^{-2} T_1^{\alpha_L}, \\ r_c &= r_{c0} h_{70}^{-1} T_1^{\alpha_r}, \end{aligned} \quad (6)$$

where $L_{X0} = 2.76 \cdot 10^{45} \text{ergs}^{-1}$, $\alpha_L = 2.56$, $r_{c0} = 223 \text{kpc}$ and $\alpha_r = 1.32$. (Note, that various authors obtain values of α_L in the range $\approx 2.5 - 3$, e.g. Markevitch 1998; Arnaud & Evrard 1999; Reiprich & Bohringer 2002).

In what follows, we give expressions for the nonthermal emission as function of T , β , r_c , and L_X . We also give expressions which depend on T and β only, using the correlations given in eq. (6). The following cautionary note should be made in this context. Our demonstration in

§ 5, that $\beta_{\text{core}} \simeq \eta_p/200$ with weak dependence on cluster mass, is based on a model that does not include entropy changes not induced by LSS shocks. As explained there, and also in § 1, early (high redshift) entropy injection (which does not significantly affect massive clusters) may modify the value of β_{core} for low mass clusters, thus introducing at low T an additional, implicit, dependence on T through β_{core} . Note, that such early entropy injections are believed to be responsible for the deviations at low T of the observed correlations, eq. (6), from the self-similar relations expected when entropy changes not induced by LSS shocks are neglected (e.g. $L_X \propto T^2$, see Arnaud & Evrard 1999).

We define the cluster mass, M_{200} , as the mass contained within a radius r_{200} , within which the mean density is 200 times the critical density, ρ_{crit} . This mass may be related to T and β by assuming the ICM plasma to be isothermal and in hydrostatic equilibrium. Under these assumptions, the gravitational mass is given by

$$M(< r) = \frac{3\beta T}{\mu m_p G} \frac{r^3}{r_c^2 + r^2} \quad (7)$$

(the mean molecular weight is $\mu \simeq 0.59$ for fully ionized plasma with hydrogen mass fraction $\chi = 0.75$), and we obtain (assuming $r_{200} \gg r_c$)

$$\begin{aligned} r_{200} &\simeq \left(\frac{800\pi}{3} \rho_{\text{crit}} \right)^{-1/2} \left(\frac{3\beta T}{\mu m_p G} \right)^{1/2} \\ &= 3.1 \beta^{1/2} T_1^{1/2} h_{70}^{-1} \text{ Mpc}, \\ M_{200} &\simeq \left(\frac{800\pi}{3} \rho_{\text{crit}} \right)^{-1/2} \left(\frac{3\beta T}{\mu m_p G} \right)^{3/2} \\ &= 3.5 \cdot 10^{15} \beta^{3/2} T_1^{3/2} h_{70}^{-1} M_{\odot}. \end{aligned} \quad (8)$$

In addition to the assumption that the ICM is isothermal and in hydrostatic equilibrium, we have extrapolated here the surface brightness given by eq. (5) out to r_{200} , which may be larger than r_X . This implies $\rho \propto r^{-2}$ at large radii, in contrast with the $\rho \propto r^{-3}$ dependence expected at large r (e.g. Navarro et al. 1997). The detailed discussion given in Reiprich & Bohringer (2002) of the accuracy of cluster mass determination under these approximations shows that eq. (8) may overestimate M_{200} by no more than 20%.

2.2. π^0 decay emission

In this section we present our model results for the emission from π^0 decays. Since the CR proton spectrum is flat, the p-p γ -ray luminosity per logarithmic photon energy bin, νL_{ν}^{pp} , is energy independent above $\sim 0.1 \text{ GeV}$ (the threshold energy for pion production is $\varepsilon_{\text{th}} \simeq 1.22 \text{ GeV}$ and the photon energy is ~ 0.1 of the parent CR proton energy). The observed spectrum is expected to be cut off at high energy due to pair production interactions of the high energy photons with infra-red background photons. For nearby clusters, the $\gamma\gamma \rightarrow e^+e^-$ cutoff is expected at $\sim 10 \text{ TeV}$ (Franceschini et al. 2008). The π^0 luminosity is given by (see eq. (A3))

$$\begin{aligned} \nu L_{\nu}^{\text{pp}} &\simeq 1.3 \cdot 10^{41} \beta_{\text{core},-4} T_1^{1/2} \\ &\times \left(\frac{L_X}{h_{70}^{-2} 3 \cdot 10^{45} \text{ erg s}^{-1}} \right) \text{ erg s}^{-1}, \end{aligned} \quad (9)$$

where $\beta_{\text{core},-4} = \beta_{\text{core}}/10^{-4}$. νL_{ν}^{pp} depends linearly on L_X , since both hadronic emission and thermal bremsstrahlung emission depend on density squared (Katz & Waxman 2008). Using the correlations eq. (6) we have

$$\nu L_{\nu}^{\text{pp}} \simeq 1.2 \cdot 10^{41} \beta_{\text{core},-4} T_1^{3.06} \text{ erg s}^{-1}. \quad (10)$$

The p-p γ -ray surface brightness above some energy $\varepsilon_{\nu, \text{min}}$ at some distance $\bar{r} \equiv r/r_c$ from the cluster center is given by (for $\beta > 0.5$, see eq. (A5) and Sarazin & Bahcall 1977)

$$\begin{aligned} S_{\nu > \nu_{\text{min}}}^{\text{pp}}(\bar{r}) &\simeq 5.5 \cdot 10^{-7} \left(3\beta - \frac{3}{2} \right) \beta_{\text{core},-4} T_1^{1/2} \\ &\times \left(\frac{L_X}{h_{70}^{-2} 3 \cdot 10^{45} \text{ erg s}^{-1}} \right) \left(\frac{r_c}{h_{70}^{-1} 200 \text{ kpc}} \right)^{-2} \\ &\times \left(\frac{\max(\varepsilon_{\nu, \text{min}}, 0.1 \varepsilon_{\text{th}})}{10 \text{ GeV}} \right)^{-1} \\ &\times (1 + \bar{r}^2)^{-3\beta+1/2} \text{ ph cm}^{-2} \text{ s}^{-1} \text{ sr}^{-1}. \end{aligned} \quad (11)$$

Using the correlations eq. (6) we have

$$\begin{aligned} S_{\nu > \nu_{\text{min}}}^{\text{pp}}(\bar{r}) &\simeq 4.1 \cdot 10^{-7} \left(3\beta - \frac{3}{2} \right) \beta_{\text{core},-4} T_1^{0.42} \\ &\times \left(\frac{\max(\varepsilon_{\nu, \text{min}}, 0.1 \varepsilon_{\text{th}})}{10 \text{ GeV}} \right)^{-1} \\ &\times (1 + \bar{r}^2)^{-3\beta+1/2} \text{ ph cm}^{-2} \text{ s}^{-1} \text{ sr}^{-1}. \end{aligned} \quad (12)$$

Note, that in the derivation of the surface brightness given above we have neglected the variation of $\beta_{\text{CR,p}}$ with radius, and used $\beta_{\text{CR,p}} = \beta_{\text{core}}$. This is justified since the surface brightness S is $\propto \beta_{\text{CR,p}} \rho_{\text{gas}}^{(6\beta-1)/3\beta}$, and, as we show in § 5, $\beta_{\text{CR,p}} \propto \rho_{\text{gas}}^{-1/3}$. This implies that the variation of the surface brightness is dominated by the $\rho_{\text{gas}}^{(6\beta-1)/3\beta}$ term (for typical β values, which are in the range of 0.5 to 1).

2.3. Emission from charged secondaries

p-p collisions also produce secondary electrons and positrons, which cool by emitting synchrotron radiation and by IC scattering of CMB photons. Since variations in the secondary injection and in the cluster magnetic field occur on time scales similar to, or larger than, the dynamical time scale of the cluster, $t_{\text{dyn}} \sim 1 \text{ Gyr}$, the distribution of secondaries is in a steady state at high energies, at which the secondaries lose all their energy to radiation on a time scale short compared to the cluster dynamical time. For magnetic field values of $1 - 10 \mu\text{G}$, the Lorentz factor of secondaries with cooling time, $6\pi m_e c / (B^2 + B_{\text{CMB}}^2) \sigma_T \gamma$, which equals the dynamical time, is $200 \lesssim \gamma_{\text{cool}} \lesssim 2000$.

The luminosity due to IC scattering of CMB photons by secondaries is given by (see eq. (A8))

$$\begin{aligned} \nu L_{\nu}^{\text{IC}, e^{\pm}} &\simeq 3.3 \cdot 10^{40} \frac{B_{\text{CMB}}^2}{B_{\text{CMB}}^2 + B^2} \beta_{\text{core},-4} T_1^{1/2} \\ &\times \left(\frac{L_X}{h_{70}^{-2} 3 \cdot 10^{45} \text{ erg s}^{-1}} \right) \text{ erg s}^{-1}. \end{aligned} \quad (13)$$

Eq. (13) holds for photon energies in the range $\gamma_{\text{cool}}^2 3T_{\text{CMB}}(1+z)^4 < \varepsilon_{\text{ph}} < \gamma_{\text{max}}^2 3T_{\text{CMB}}(1+z)^4$, where

$\gamma_{\max} \simeq 0.1 \varepsilon_{\max} / m_e c^2$ (ε_{\max} is the maximal energy of the CR protons, and the secondary energy is ~ 0.1 of the parent proton energy). The surface brightness is given by (see eq. (A9))

$$S_{\nu > \nu_{\min}}^{\text{IC}, e^\pm}(\bar{r}) \simeq 1.4 \cdot 10^{-7} \left(3\beta - \frac{3}{2}\right) \frac{B_{\text{CMB}}^2}{B_{\text{CMB}}^2 + B^2} \\ \times \beta_{\text{core}, -4} T_1^{1/2} \left(\frac{L_X}{h_{70}^{-2} 3 \cdot 10^{45} \text{ erg s}^{-1}}\right) \\ \times \left(\frac{r_c}{h_{70}^{-1} 200 \text{ kpc}}\right)^{-2} \left(\frac{\varepsilon_{\nu, \min}}{10 \text{ GeV}}\right)^{-1} \\ \times (1 + \bar{r}^2)^{-3\beta+1/2} \text{ ph cm}^{-2} \text{ s}^{-1} \text{ sr}^{-1}. \quad (14)$$

Using the correlations eq. (6) we have

$$\nu L_\nu^{\text{IC}, e^\pm} \simeq 3.0 \cdot 10^{40} \frac{B_{\text{CMB}}^2}{B_{\text{CMB}}^2 + B^2} \\ \times \beta_{\text{core}, -4} T_1^{3.06} \text{ erg s}^{-1}, \quad (15)$$

and

$$S_{\nu > \nu_{\min}}^{\text{IC}, e^\pm}(\bar{r}) \simeq 1.0 \cdot 10^{-7} \left(3\beta - \frac{3}{2}\right) \frac{B_{\text{CMB}}^2}{B_{\text{CMB}}^2 + B^2} \\ \times \beta_{\text{core}, -4} T_1^{0.42} \left(\frac{\varepsilon_{\nu, \min}}{10 \text{ GeV}}\right)^{-1} \\ \times (1 + \bar{r}^2)^{-3\beta+1/2} \text{ ph cm}^{-2} \text{ s}^{-1} \text{ sr}^{-1}. \quad (16)$$

Note that although the γ -ray luminosity produced by π^0 decays is bigger above $\sim 0.1 \text{ GeV}$ by a factor $\simeq 4(1 + B^2/B_{\text{CMB}}^2)$ than that produced by charged secondaries (compare eq. (9) and eq. (13)), the secondaries' emission is the main hadronic emission mechanism below this energy.

For photons in the energy range $\gamma_{\text{cool}}^2 \varepsilon_0 < \varepsilon_{\text{ph}} < \gamma_{\text{max}}^2 \varepsilon_0$, where $\varepsilon_0 = 3\hbar e B / 2m_e c$, the secondary synchrotron luminosity from is given by (see eq. (A12))

$$\nu L_\nu^{\text{sync}, e^\pm} \simeq 3.3 \cdot 10^{40} \frac{B^2}{B_{\text{CMB}}^2 + B^2} \beta_{\text{core}, -4} T_1^{1/2} \\ \times \left(\frac{L_X}{h_{70}^{-2} 3 \cdot 10^{45} \text{ erg s}^{-1}}\right) \text{ erg s}^{-1}, \quad (17)$$

and the surface brightness is (see eq. (A13))

$$S_\nu^{\text{sync}, e^\pm}(\bar{r}) \simeq 13 \cdot \left(3\beta - \frac{3}{2}\right) \frac{B^2}{B_{\text{CMB}}^2 + B^2} \\ \times \beta_{\text{core}, -4} T_1^{1/2} \left(\frac{L_X}{h_{70}^{-2} 3 \cdot 10^{45} \text{ erg s}^{-1}}\right) \\ \times \left(\frac{r_c}{h_{70}^{-1} 200 \text{ kpc}}\right)^{-2} \left(\frac{\nu}{1.4 \text{ GHz}}\right)^{-1} \\ \times (1 + \bar{r}^2)^{-3\beta+1/2} \text{ mJy arcmin}^{-2}. \quad (18)$$

Using the correlations eq. (6) we have

$$\nu L_\nu^{\text{sync}, e^\pm} \simeq 3.0 \cdot 10^{40} \frac{B^2}{B_{\text{CMB}}^2 + B^2} \beta_{\text{core}, -4} \\ \times T_1^{3.06} \text{ erg s}^{-1}, \quad (19)$$

and

$$S_\nu^{\text{sync}, e^\pm}(\bar{r}) \simeq 9.8 \cdot \left(3\beta - \frac{3}{2}\right) \frac{B^2}{B_{\text{CMB}}^2 + B^2} \\ \times \beta_{\text{core}, -4} T_1^{0.42} \left(\frac{\nu}{1.4 \text{ GHz}}\right)^{-1} \\ \times (1 + \bar{r}^2)^{-3\beta+1/2} \text{ mJy arcmin}^{-2}. \quad (20)$$

Note, that due to the uncertainties in B and t_{dyn} , which lead to uncertainty in γ_{cool} , our estimates of the emission from secondary electrons and positrons with $\gamma \sim \gamma_{\text{cool}}$ are uncertain.

2.4. Primary electron emission

We now turn to estimating the radiation produced by primary electrons at the accretion shock. We assume that the clusters are spherical and that gas is accreted onto clusters in spherically symmetric flows at a rate $\dot{M} = f_{\text{inst}} M_{200} / t_H$. f_{inst} is a dimensionless parameter of order unity, reflecting the temporal fluctuations of $\dot{M} / (M_{200} / t_H)$. As discussed in § 3, 3D numerical simulations indicate that the average value of f_{inst} is ≈ 0.5 .

In order to calculate the surface brightness of the primary electrons' radiation, it is necessary to estimate the position of the accretion shock. We assume here that the accretion shock is located at $r \sim r_{200}$, since spherical collapse models predict a cluster virial density $< \rho_{\text{vir}} > \simeq 178 \rho_{\text{crit}}$ (for $\Omega_m = 1$ and $\Omega_\Lambda = 0$, with weak dependance on the background cosmology for $0.3 \lesssim \Omega_m < 1$). The validity of the simplifying assumptions described above is tested in § 3 by comparing our results to those of numerical 3D simulations. We find that the results obtained in this section are in good agreement with the results of detailed numerical simulations.

As in the case of the charged secondaries, we assume that the distribution of the primaries is in a steady state, since electrons (at the relevant energies) lose all their energy to radiation on a time scale short compared to the cluster dynamical time, $t_{\text{dyn}} \sim 1 \text{ Gyr}$. Unlike the secondary electrons and positrons, which lose energy through both IC and synchrotron emission, primary electrons lose their energy mainly by IC scattering of CMB photons, since the magnetic field at the accretion shock is expected to be weak, $\sim 0.1 \mu\text{G} \ll B_{\text{CMB}}$ (Waxman & Loeb 2000). Thus the steady state assumption holds for primaries with Lorenz factors $\gamma > \gamma_{\text{cool}} \sim 2000$. The maximal energy of the primary electrons is determined by equating the acceleration time, $r_{L,e} c / v_{\text{sh}}^2 \simeq 1.6 \cdot 10^3 \gamma_7 (B_{-7} T_1)^{-1} \text{ yr}$ (where $r_{L,e} = 5.5 \cdot 10^{-2} \gamma_7 / B_{-7} \text{ pc}$ is the Larmor radius of the electron), to the IC cooling time, $6\pi m_e c / B_{\text{CMB}}^2 \sigma_T \gamma \simeq 2.3 \cdot 10^5 \gamma_7^{-1} (1+z)^{-4} \text{ yr}$, which yields $\gamma_{\max} \simeq 1.2 \cdot 10^8 \sqrt{B_{-7} T_1} (1+z)^{-2}$.

For photon energies $\gamma_{\text{cool}}^2 3T_{\text{CMB}}(1+z)^4 < \varepsilon_{\text{ph}} < \gamma_{\text{max}}^2 3T_{\text{CMB}}(1+z)^4$, the primary IC luminosity is given, to very good accuracy, by (see eq. (A16) and eq. (A17))

$$\nu L_\nu^{\text{IC}, \text{shock}} \simeq 1.8 \cdot 10^{43} (f_{\text{inst}} \eta_e)_{-2} \beta^{3/2} \\ \times \left(\frac{f_b}{0.17}\right) T_1^{5/2} \bar{Z}(z) \text{ erg s}^{-1}. \quad (21)$$

Here, $(f_{\text{inst}} \eta_e)_{-2} = f_{\text{inst}} \eta_e / 10^{-2}$, $f_b = \Omega_b / \Omega_m$ and $\bar{Z}(z) \equiv (t_H H(z))^{-1}$ ($\bar{Z}(z)$ depends weakly on the assumed cosmology). Assuming the emission originates from a thin layer with thickness w behind the accretion shock, the surface brightness is given by

$$S_{\nu > \nu_{\min}}^{\text{IC}, \text{shock}}(r) \simeq 1.5 \cdot 10^{-7} (f_{\text{inst}} \eta_e)_{-2} \beta^{1/2} \\ \times \left(\frac{f_b}{0.17}\right) T_1^{3/2} \left(\frac{\varepsilon_{\nu, \min}}{10 \text{ GeV}}\right)^{-1} \\ \times \xi(r/r_{200}, w/r_{200}) \\ \times \bar{Z}(z) h_{70}^2(z) \text{ ph cm}^{-2} \text{ s}^{-1} \text{ sr}^{-1}, \quad (22)$$

where

$$\xi(x, y) = \begin{cases} \frac{3(\sqrt{1-x^2} - \sqrt{(1-y)^2 - x^2})}{1 - (1-y)^3}, & x \leq 1 - y \\ \frac{3\sqrt{1-x^2}}{1 - (1-y)^3}, & 1 - y < x < 1. \end{cases} \quad (23)$$

For $w \ll r_{200}$, $\xi(x, y)$ can be approximated in the regime $x < 1 - y$ by

$$\xi(x, y) \simeq \frac{1}{\sqrt{1-x^2}}. \quad (24)$$

The thickness w of the emitting region is approximately given by the product of the cooling time of the emitting electrons, t_{cool} , and the velocity of the downstream fluid relative to the shock velocity, u_d . Since $t_{\text{dyn}} \sim r_{200}/u_d$, the approximation $w \ll r_{200}$ holds for $\gamma > \gamma_{\text{cool}} \sim 2000$. Note that the rapid increase of the surface brightness near the accretion shock, inferred from eq. (24), is likely to be suppressed by small deviations from spherical symmetry.

Below ~ 1 TeV, the primary IC γ -ray luminosity is larger than the secondary γ -ray luminosity by a factor $\simeq 150(f_{\text{inst}}\eta_e)_{-2}(\beta_{\text{core}})_{-4}^{-1}\beta^{3/2}T_1^{-1/2}$ (compare eq. (21) to the neutral component contribution eq. (10), which dominates the secondary emission at this energy range). The primary IC HXR luminosity is larger than the secondary HXR luminosity by a factor $\simeq 600(f_{\text{inst}}\eta_e)_{-2}(\beta_{\text{core}})_{-4}^{-1}\beta^{3/2}T_1^{-1/2}(1 + B^2/B_{\text{CMB}}^2)$ (compare eq. (21) to the charged component contribution eq. (15), which dominates the secondary emission at this energy range). However, since the primary electrons' IC surface brightness is lowest at the cluster core, while the secondaries' emission surface brightness follows the thermal surface brightness (see e.g. eq. (11)), the surface brightness due to these two sources of radiation may be comparable at the cluster core.

For photon energies $\gamma_{\text{cool}}^2 \varepsilon_0 < \varepsilon_{\text{ph}} < \gamma_{\text{max}}^2 \varepsilon_0$, the primary electrons' synchrotron luminosity is given by (see eq. (A20))

$$\begin{aligned} \nu L_{\nu}^{\text{sync,shock}} &\simeq 1.7 \cdot 10^{40} (f_{\text{inst}}\eta_e)_{-2} \beta^{3/2} \\ &\times \left(\frac{f_b}{0.17}\right) T_1^{5/2} B_{-7}^2 \\ &\times \bar{Z}(z)(1+z)^{-4} \text{erg s}^{-1}. \end{aligned} \quad (25)$$

This luminosity is comparable to the luminosity produced by secondaries. However, the primary electron synchrotron surface brightness,

$$\begin{aligned} S_{\nu}^{\text{sync,shock}}(r) &\simeq 1.4 \cdot 10^{-2} (f_{\text{inst}}\eta_e)_{-2} \beta^{1/2} \\ &\times \left(\frac{f_b}{0.17}\right) T_1^{3/2} \left(\frac{\nu}{1.4 \text{ GHz}}\right)^{-1} \\ &\times B_{-7}^2 \xi(r/r_{200}, w/r_{200}) \bar{Z}(z) \\ &\times h_{70}^2(z)(1+z)^{-4} \text{mJy arcmin}^{-2} \end{aligned} \quad (26)$$

(see eq. (A21)), is negligible compared to that produced by secondaries (see eq. (18)).

2.5. Summary of results

Figure 1 shows the nonthermal luminosity, νL_{ν} , as function of photon energy for a $T = 10$ keV, $\beta = 2/3$ cluster (with L_X and r_c determined by eq. (6)), with

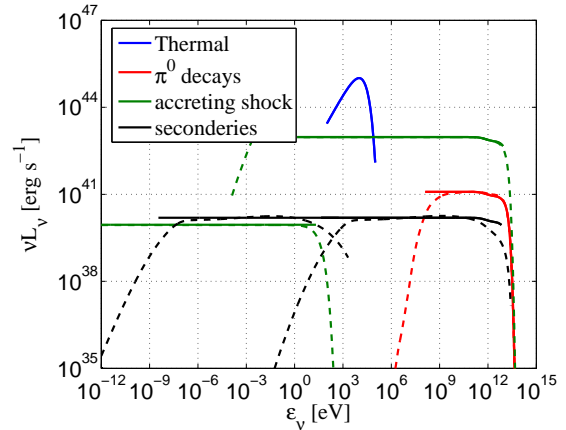


FIG. 1.— νL_{ν} as function of photon energy for a $T = 10$ keV, $\beta = 2/3$ cluster, with $\beta_{\text{core}} = 10^{-4}$, $f_{\text{inst}}\eta_e = 0.01$, $B = B_{\text{CMB}}$ at the cluster core and $B = 0.1 \mu\text{G}$ at the accretion shock. Solid lines show the simple estimates given by eqs. (9), (13), (17), (21) and (25), and dashed lines are obtained using the parametrization of Kamae et al. (2006) for the secondary spectrum of p-p interactions, and the exact formulae for IC scattering and synchrotron emission given by Blumenthal & Gould (1970). Suppression of the flux by pair production (in interactions with IR background photons) was included, applying a suppression factor $\exp(-\tau_{\gamma\gamma})$ with pair production optical depth (taken from Franceschini et al. 2008) corresponding to a cluster at the distance of Coma. Note, that there is an artificial high energy cut-off in the secondary emission spectra calculated using the parametrization of Kamae et al. (2006), resulting from the upper limit on the proton energy used in this parametrization, 512 TeV.

$\beta_{\text{core}} = 10^{-4}$, $f_{\text{inst}}\eta_e = 0.01$, $B = B_{\text{CMB}}$ at the cluster core and $B = 0.1 \mu\text{G}$ at the accretion shock (for our assumed background cosmology we have $\bar{Z}(z=0) \simeq 0.97$). Solid lines show the simple estimates given above by eqs. (9), (13), (17), (21) and (25), and the dashed lines are obtained using the parametrization of Kamae et al. (2006) for the secondary spectrum of p-p interactions, and the exact formulae for IC scattering and synchrotron emission given by Blumenthal & Gould (1970). Suppression of the flux by pair production (in interactions with IR background photons) was included, applying a suppression factor $\exp(-\tau_{\gamma\gamma})$ with pair production optical depth (taken from Franceschini et al. 2008) corresponding to a cluster at the distance of Coma. Note, that there is an artificial high energy cut-off in the secondary emission spectra calculated using the parametrization of Kamae et al. (2006), resulting from the upper limit on the proton energy used in this parametrization, 512 TeV. However, the secondaries' emission is always small in this range compared to other emission processes.

In fig. 2 we show HXR, γ -ray and radio surface brightness profiles for the same cluster at various energies (see eqs. (11), (14), (18), (22) and (26)). The thickness of the layer behind the accretion shock, from which the primary electron emission originates, is estimated to be $w \simeq u_d t_{\text{cool}}$. For the chosen cluster parameters, the dominant nonthermal emission process in the HXR (> 100 keV) band is IC emission from primary electrons at the accretion shock. At higher photon energies (> 10 GeV) the emission from pion decays at the core of the cluster becomes comparable to the IC emission from the accretion shock electrons. Note, that the IC emission from accretion shock electrons is uncertain at

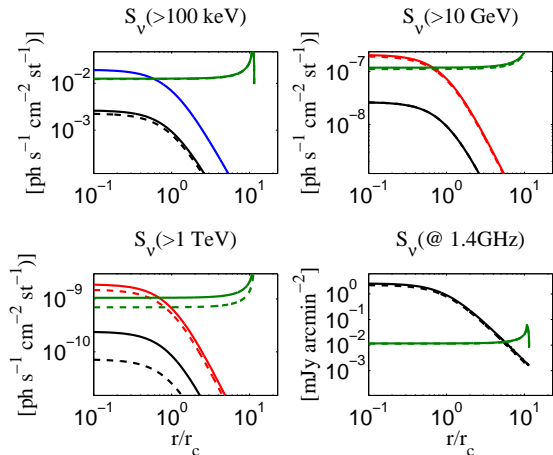


FIG. 2.— HXR, γ -ray and radio surface brightness as function of radius, given by eqs. (11), (14), (18), (22) and (26). Cluster parameters and line types are the same as in fig. 1. The thickness of the layer behind the accretion shock, from which the primary electron emission originates, is estimated to be $w \simeq u_d t_{\text{cool}} \ll r_{200}$. Note that the rapid increase of the surface brightness near the accretion shock is likely to be suppressed by small deviations from spherical symmetry.

energies exceeding ~ 1 TeV, due to the uncertainty in the maximal energy, \sim few TeV, to which electrons may be accelerated in such shocks. Thus, although at the figures shown the IC emission dominates the luminosity also at the highest energies, > 1 TeV, pion decays may become the dominant emission process at these energies. At all energies, the contribution from secondary IC is small. However, the synchrotron emission of secondaries is the dominant emission process at the radio band.

3. COMPARISON TO DETAILED NUMERICAL SIMULATIONS

In this section we compare our model's results with a variety of detailed numerical simulations. We show that our results are in agreement with those of numerical simulations, with the exception of deviations which are due to inaccuracies of the numerical calculations.

Keshet et al. (2003) used TreeSPH simulations of LSS formation to estimate the IC emission from electrons accelerated in LSS shocks. The typical > 10 GeV flux from rich clusters obtained by Keshet et al. (2003) is $\text{few} \times 10^{-7} (\eta_e/0.05) \text{ ph cm}^{-2} \text{ s}^{-1} \text{ sr}^{-1}$ (see their fig. 10), consistent with the prediction of eq. (22). Keshet et al. (2003) also used the simulations to determine $N(> f)$, the number of sources expected with flux exceeding f (at a given photon energy threshold). The model presented here for the nonthermal emission of clusters may be used to predict $N(> f)$ for a given number density of halos as function of redshift and halo mass. Such an exercise has already been carried out by Waxman & Loeb (2000), who derived analytic expressions for the γ -ray luminosity of primary electrons and used them to predict $N(> f)$ assuming a Press-Schechter (Press & Schechter 1974) mass function for the cluster halo density. The expressions derived here for the gamma-ray luminosity of a cluster of a given mass are identical, up to a normalization factor, to those of Waxman & Loeb (2000), implying that our prediction for $N(> f)$ would be similar to that of Waxman & Loeb (2000). Since in the normalization used

by Waxman & Loeb (2000) the accretion rate is $\sim 3f_{\text{inst}}^{-1}$ larger than the one used here, and since the IC accretion luminosity is proportional to the accretion rate, the luminosity function, $N(> f)$, obtained using our normalization is related to the one derived by Waxman & Loeb (2000), $N_{\text{WL}}(> f)$, by $N(> f) = N_{\text{WL}}(> 3f_{\text{inst}}^{-1}f)$. Keshet et al. (2003) found that their numerical source number counts, $N_{\text{num}}(> f)$, fall short of the analytical prediction of Waxman & Loeb (2000) by a factor of ~ 6 , in the sense that $N_{\text{num}}(> f) \approx N_{\text{WL}}(> 6f)$. This implies that the analysis presented here is consistent with the numerical number counts of Keshet et al. (2003) for $f_{\text{inst}} \simeq 0.5$.

The results of TreeSPH simulations of LSS evolution incorporating CR generation in LSS shocks were recently reported in a series of papers (Pfrommer et al. 2007, 2008; Pfrommer 2008). In these simulations, $\eta_p = 0.5$ and $\eta_e = 0.05$ were adopted, and the CR evolution was followed under the assumption that the CR energy spectrum is a power-law. Figure 3 presents a comparison of our results with those obtained by Pfrommer et al. (2008) for a massive ($M = 10^{15} M_{\odot}$, $T = 9.6$ keV) merging cluster, for which detailed emission spectra are given. The simulation's surface brightness profiles of pion decay and secondary IC emission above 100 MeV follow the thermal surface brightness with central values of $S_{\nu}^{\text{PP}}(0) \simeq 5 \cdot 10^{-4} \text{ ph cm}^{-2} \text{ s}^{-1} \text{ sr}^{-1}$ and $S_{\nu}^{\text{IC},e^{\pm}}(0) \simeq 5 \cdot 10^{-5} \text{ ph cm}^{-2} \text{ s}^{-1} \text{ sr}^{-1}$ respectively. The profiles and the central values of the surface brightness of pion decay and secondary IC emission obtained in the simulation are consistent (to within a factor of two) with those predicted by eqs. (12) and (16) for $\beta_{\text{core}} = 2 \cdot 10^{-3}$ and $\beta = 2/3$. This value of β_{core} is consistent with our simple model prediction, $\beta_{\text{core}} \approx \eta_p/200$, for the value of η_p chosen in the simulations, $\eta_p = 0.5$. The ratio of pion decay to secondary IC luminosity obtained in the simulation is larger than predicted by our model. This may be a result of using power-law approximations for the CR emission spectra (compare the solid and dashed lines of our model near 100 MeV in figs. 1, 3). We note that the numerical calculations, to which our model predictions are compared in fig. 3, included radiative cooling of the ICM plasma, which is not included in our model. As explained in § 5.4, such radiative cooling is not expected to significantly affect the nonthermal emission of massive clusters. This conclusion is consistent with the results of the numerical calculations (see, e.g., fig. 13 in Pfrommer et al. 2008).

The value of β_{core} obtained in the simulation for the cluster used for the comparison of fig. 3 can not be easily extracted from the results reported, since a profile of the ratio of CR to thermal gas pressure is not given. Instead, a profile of CR to thermal gas pressure ratio averaged over 9 clusters, including the one used for the comparison of fig. 3 and 8 smaller ($5 \cdot 10^{13} - 5 \cdot 10^{14} M_{\odot}$) clusters, is given. This averaged pressure ratio profile is nearly constant throughout the cluster at a value of ~ 0.1 , and rises sharply within the inner 2% of the virial radius to ~ 1 . A pressure ratio of ~ 0.1 corresponds (for $\eta_p = 0.5$) to $\beta_{\text{core}}/\eta_p \approx 2/100$, larger than inferred by our analysis. However, this profile is probably biased towards larger values of $\beta_{\text{core}}/\eta_p$ due to the large number of small clusters for which radiative cooling is

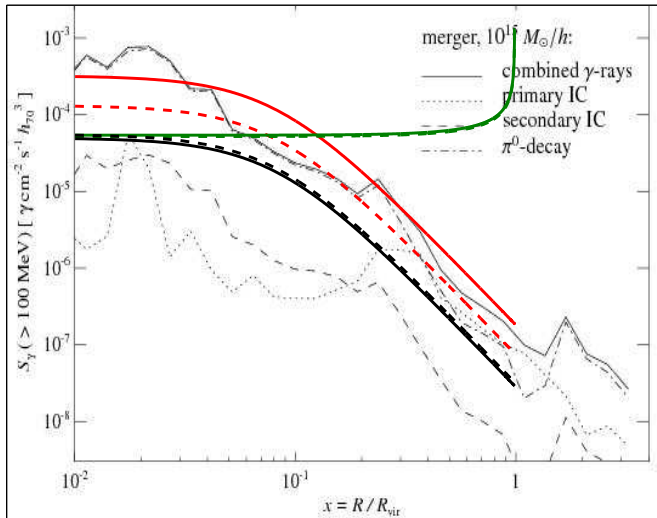


FIG. 3.— Figure 12 of Pfrommer et al. (2008) (courtesy of C. Pfrommer). Over plotted are the surface brightness curves obtained from our simple analysis (eqs. (11), (14) and (22)), for a $T = 9.4$ keV, $\beta = 2/3$ cluster with $\beta_{\text{core}} = 2 \cdot 10^{-3}$, $\eta_e = 0.05$ (as chosen in the simulation), and $f_{\text{inst}} = 1$ (L_X and r_c were determined according to eq. (6)). $\beta_{\text{core}} = 2 \cdot 10^{-3}$ is consistent with our model prediction, $\beta_{\text{core}} \approx \eta_p/200$, for the value of η_p chosen in the simulation, $\eta_p = 0.5$. Line types are the same as in fig. 1. Note that the rapid increase of the (primary) surface brightness near the accretion shock is likely to be suppressed by small deviations from spherical symmetry.

more important (radiative cooling also leads to the sharp rise at the inner 2% of the virial radius). By examining the pressure ratio profiles of $M \sim 10^{14} M_\odot$ clusters in the non-radiative simulations, which should be very similar to those of more massive clusters (see also table 3 in Pfrommer et al. 2007), we find that indeed this ratio decreases toward the center of the cluster to a value $\beta_{\text{core}}/\eta_p \sim 1/500$.

The primary electrons' IC surface brightness obtained in the simulation is approximately uniform across the cluster. Its value, $S_\nu^{\text{IC,shock}} \simeq 5 \cdot 10^{-6} \text{ ph cm}^{-2} \text{ s}^{-1} \text{ sr}^{-1}$, is lower by a factor of $\simeq 10$ compared to the prediction of eq. (22) (for $\beta = 2/3$ and $f_{\text{inst}} = 1$). This discrepancy is due to the fact that the accretion shock is located at the simulation at a radius of ~ 10 Mpc, ~ 3 times larger than r_{200} (see eq. (8)), where we assume the shock to be located. That is, the total primary IC luminosity obtained in the simulation is in agreement with our prediction, eq. (21), but the surface brightness is ~ 10 times lower since the shock is located in the simulation at a ~ 3 times larger radius. We believe that the shock radius is overestimated in the simulation, since our results are consistent with those of the numerical simulations of both Keshet et al. (2003) and Miniati (2003) (see below), which imply the shock position to be closer to r_{200} than obtained by Pfrommer et al. (2007). Moreover, Molnar et al. (2009) have recently shown that accretion shocks are located in SPH simulations at a radius which is $\simeq 3$ larger than that obtained in AMR simulations, probably due to numerical inaccuracies in the SPH simulations.

Figure 4 presents a graphical comparison of our results with those of Miniati (2003), who modelled the evolution of CR protons and electrons using an Eulerian+N-

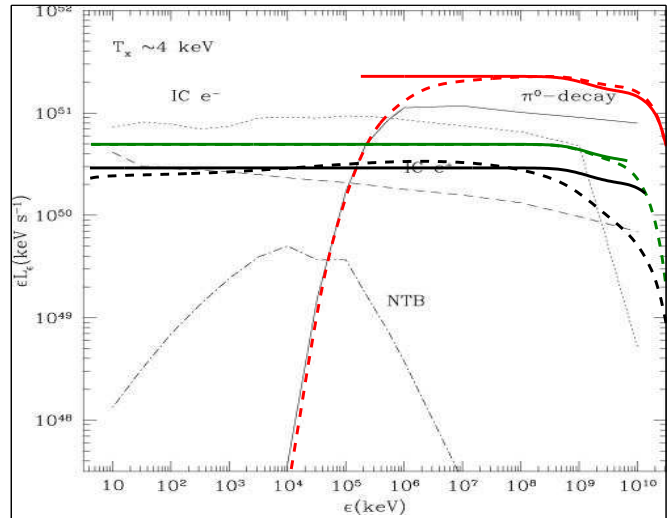


FIG. 4.— Figure 2 from Miniati (2003) (courtesy of F. Miniati). Over plotted are νL_ν curves obtained from our simple analysis (eqs. (9), (13) and (21)), for a $T = 4$ keV and $\beta = 2/3$ cluster with $\beta_{\text{core}} = 0.05$, $\eta_e = 0.01$ (as chosen in the simulation), and $f_{\text{inst}} = 1$ (L_X and r_c were determined according to eq. (6)). The large value of β_{core} obtained in the simulations is probably due to the low resolution of the simulation (see text). Line types are the same as in fig. 1.

body code to describe the evolution of the LSS, assuming CRs are generated at strong shocks with $\eta_p \sim 0.6$ and $\eta_e = 0.01$. The IC luminosity of primary electrons obtained by Miniati (2003), $\nu L_\nu^{\text{IC,shock}} \simeq 2 \cdot 10^{42} \text{ erg s}^{-1}$, is consistent with the prediction of eq. (21) (for $\beta = 2/3$ and $f_{\text{inst}} = 1$). The value of β_{core} obtained in the simulation, $\beta_{\text{core}} \sim 0.05$ for a $T = 4$ keV cluster, implies a ratio $\beta_{\text{core}}/\eta_p \sim 1/10$, significantly larger than the value we estimated, $\simeq 1/200$, which is consistent with the results of the Pfrommer et al. (2007) simulations. This discrepancy is most likely due to the low, ~ 100 kpc, resolution of the simulation of Miniati (2003), which doesn't allow one to properly resolve the adiabatic compression at the core. The pion decay luminosity and the secondaries' IC luminosity obtained by Miniati (2003) are $\nu L_\nu^{\text{PP}} \simeq 2 \cdot 10^{42} \text{ erg s}^{-1}$ and $\nu L_\nu^{\text{IC,e}^\pm} \simeq 5 \cdot 10^{41} \text{ erg s}^{-1}$ respectively. Both are comparable to our model predictions, eqs. (10) and (15), for $T = 4$ keV and $\beta_{\text{core}} = 0.05$.

4. COMPARISON TO OBSERVATIONS - THE COMA CLUSTER

In this section we compare the results of our analytic model to various observations of the Coma cluster. We use these observations to test our model and to constrain its parameters. For the comparison, we use the following parameters to characterize the Coma cluster: $T_{\text{Coma}} = 8.25$ keV, $L_{X,\text{Coma}} = 1.1 \cdot 10^{45} h_{70}^{-2} \text{ erg s}^{-1}$, $\beta_{\text{Coma}} = 0.654$, $r_{c,\text{Coma}} = 246 h_{70}^{-1} \text{ kpc}$, $r_{200,\text{Coma}} \simeq 2.3 h_{70}^{-1} \text{ Mpc}$, $M_{200,\text{Coma}} \simeq 1.4 \cdot 10^{15} M_\odot$ and $z_{\text{Coma}} = 0.0232$ (Reiprich & Bohringer 2002). With these parameters we have $r_{c,\text{Coma}}/d_{\text{Coma}} \simeq 0.14^\circ$ and $r_{200,\text{Coma}}/d_{\text{Coma}} \simeq 1.3^\circ$, where d_{Coma} is the distance to the Coma cluster. Note that the surface brightness measurements of Reiprich & Bohringer (2002) reach $r_{X,\text{Coma}} \simeq 2.9 h_{70}^{-1} \text{ Mpc} > r_{200,\text{Coma}}$, so extrapolation is not needed in order to determine r_{200} and M_{200} for this

cluster.

In order to make the comparison with observations more straightforward, we first give below explicit expressions for the flux predicted by our model within a disk of angular radius θ (centered at the cluster's center) for a cluster at a distance $d \simeq cz/H_0$. We further assume that within the cluster core $B^2 \gg B_{\text{CMB}}^2$, as inferred from radio observations (Kushnir et al. 2009), and normalize our results to $B_{-5} = B/10 \mu\text{G}$. Using the results of § 2, we have

$$\begin{aligned}
F_{\nu > \nu_{\min}}^{\text{PP}}(\theta) &= 1.4 \cdot 10^{-11} \left(3\beta - \frac{3}{2}\right) \beta_{\text{core},-4} T_1^{1/2} \\
&\times \left(\frac{L_X}{h_{70}^{-2} 3 \cdot 10^{45} \text{ erg s}^{-1}} \right) \\
&\times \int_0^{\min(\theta d/r_c, r_{200}/r_c)} (1 + \bar{r}^2)^{-3\beta+1/2} \bar{r} d\bar{r} \\
&\times \left(\frac{\max(\varepsilon_{\nu, \min}, 0.1\varepsilon_{\text{th}})}{10 \text{ GeV}} \right)^{-1} \left(\frac{z}{z_{\text{Coma}}} \right)^{-2} \\
&\times h_{70}^2 \text{ ph cm}^{-2} \text{ s}^{-1} \quad (27)
\end{aligned}$$

for γ -rays from pion decay,

$$\begin{aligned}
F_{\nu > \nu_{\min}}^{\text{IC}, e^\pm}(\theta) &= 3.4 \cdot 10^{-13} \left(3\beta - \frac{3}{2}\right) B_{-5}^{-2} \beta_{\text{core},-4} \\
&\times T_1^{1/2} \left(\frac{L_X}{h_{70}^{-2} 3 \cdot 10^{45} \text{ erg s}^{-1}} \right) \\
&\times \int_0^{\min(\theta d/r_c, r_{200}/r_c)} (1 + \bar{r}^2)^{-3\beta+1/2} \bar{r} d\bar{r} \\
&\times \left(\frac{\varepsilon_{\nu, \min}}{10 \text{ GeV}} \right)^{-1} \left(\frac{z}{z_{\text{Coma}}} \right)^{-2} \\
&\times h_{70}^2 \text{ ph cm}^{-2} \text{ s}^{-1} \quad (28)
\end{aligned}$$

for IC emission from secondaries,

$$\begin{aligned}
S_{\nu}^{\text{sync}, e^\pm}(\theta) &= 3.7 \left(3\beta - \frac{3}{2}\right) \beta_{\text{core},-4} T_1^{1/2} \\
&\times \left(\frac{L_X}{h_{70}^{-2} 3 \cdot 10^{45} \text{ erg s}^{-1}} \right) \\
&\times \int_0^{\min(\theta d/r_c, r_{200}/r_c)} (1 + \bar{r}^2)^{-3\beta+1/2} \bar{r} d\bar{r} \\
&\times \left(\frac{\nu}{1.4 \text{ GHz}} \right)^{-1} \left(\frac{z}{z_{\text{Coma}}} \right)^{-2} \\
&\times h_{70}^2 \text{ Jy} \quad (29)
\end{aligned}$$

for synchrotron emission from secondaries, and

$$\begin{aligned}
F_{\nu > \nu_{\min}}^{\text{IC}, \text{shock}}(\theta) &= 4.7 \cdot 10^{-7} (\langle f_{\text{inst}} \rangle_{\theta} \eta_e)_{-2} \beta^{1/2} \\
&\times \left(\frac{f_b}{0.17} \right) T_1^{3/2} \left(\frac{\varepsilon_{\nu, \min}}{10 \text{ GeV}} \right)^{-1} \\
&\times g_{\text{acc.}}(\theta) \bar{Z}(z) h_{70}^2(z) \text{ ph cm}^{-2} \text{ s}^{-1}, \quad (30)
\end{aligned}$$

with

$$g_{\text{acc.}}(\theta) = 2\theta_{200}^2 \left(1 - \sqrt{1 - \left(\frac{\theta}{\theta_{200}} \right)^2} \right), \quad (31)$$

for IC emission of primary electrons. Here $\theta_{200} = r_{200}/d$ and $\langle f_{\text{inst}} \rangle_{\theta}$ is the average value of f_{inst} over the disk

considered. Eq (31) gives an approximate description of the dependence of F on θ , for the case where $w \ll r_{200}$ (see eq. (24)). For $w = 0.1r_{200}$, eq. (31) is accurate to better than $\sim 25\%$.

4.1. HXR observations

An excess of HXR emission over the expected thermal bremsstrahlung emission has been observed in the Coma cluster with instruments on board three different X-ray satellites: RXTE (Rephaeli et al. 1999; Rephaeli & Gruber 2002), BeppoSax (Fusco-Femiano et al. 1999; Fusco-Femiano et al. 2004, 2007) and INTEGRAL (Eckert et al. 2007; Lutovinov et al. 2008). Since the observations are in agreement with each other, we focus on the recent INTEGRAL observations. The INTEGRAL-measured flux in the 44 – 107 keV band (where the thermal contribution is small) is $(1.8 \pm 1.1) \cdot 10^{-11} \text{ erg cm}^{-2} \text{ s}^{-1}$ within $\theta < 1^\circ$. To study the spatial structure of the HXR emission, images in the "soft" 17 – 28.5 keV and in the "hard" 44 – 107 keV INTEGRAL bands were used. In the soft band, Coma is clearly an extended source. At the hard-band, the raw image does not show any significant substructure or correlation with the cluster's thermal emission (on 1° scale). The extended nature of the HXR emission implies that the radiating particles are not secondary particles produced in the interaction of cosmic-rays with the ICM, since the generation of such secondary particles should be strongly concentrated towards the cluster's center.

In fig. 5 we show the estimated HXR flux within a disk of angular radius θ as function of θ for the Coma cluster in the 44 – 107 keV band, assuming $f_{\text{inst}}\eta_e = 0.01$, $\beta_{\text{core}} = 10^{-4}$ and $B = 10 \mu\text{G}$. The INTEGRAL measurement and the thermal emission in this band are also given. Since the nonthermal flux is dominated in this band, according to our model, by IC emission of accretion shock electrons, the observed HXR flux may be used to calibrate $\eta_e f_{\text{inst}}$ (β_{core} is not constrained since the contribution from secondaries is negligible). According to our model, the hard-band image should not show any significant substructure since it originates from the accretion shock, and no spatial correlation with the cluster thermal emission is expected.

Using eqs. (28) and (30), with $\bar{Z}(0) \simeq 0.96$ and

$$\int_0^{1^\circ/0.14^\circ} (1 + \bar{r}^2)^{-3\beta_{\text{Coma}}+1/2} \bar{r} d\bar{r} \simeq 0.90, \quad (32)$$

we have

$$\begin{aligned}
F_{\text{Coma, total}}(1^\circ) &\simeq 6.7 \cdot 10^{-16} \beta_{\text{core},-4} B_{-5}^{-2} \\
&+ 1.4 \cdot 10^{-12} (\langle f_{\text{inst}} \rangle_{1^\circ} \eta_e)_{-2} \frac{\text{erg}}{\text{cm}^2 \text{ s}} \quad (33)
\end{aligned}$$

(where we have multiplied the number flux by $\ln(\varepsilon_{\text{max}}/\varepsilon_{\text{min}})(1/\varepsilon_{\text{min}} - 1/\varepsilon_{\text{max}})^{-1}$ with $\varepsilon_{\text{min}} = 44 \text{ keV}$ and $\varepsilon_{\text{max}} = 107 \text{ keV}$, in order to obtain the energy flux). The INTEGRAL measurement thus constrains $0.06 < \langle f_{\text{inst}} \rangle_{1^\circ} \eta_e < 0.23$. Note, that our analysis also rules out secondary emission as the source of the HXR excess, since in order to reproduce the observed flux by secondary emission $\beta_{\text{core}} \sim 5$ would be required, implying that the CR energy density is much greater than the thermal energy density of the ICM.

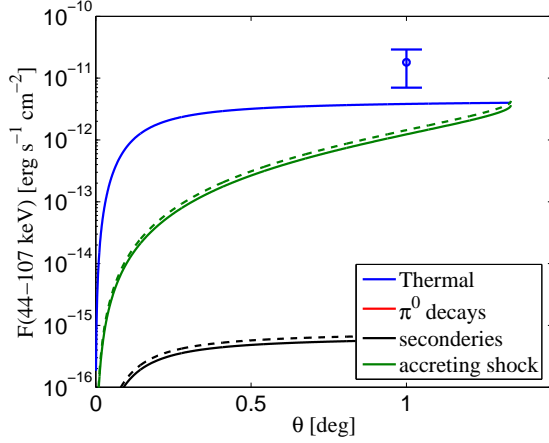


FIG. 5.— The predicted HXR flux within a disk of angular radius θ as function of θ for the Coma cluster in the 44 – 107 keV band, assuming $f_{\text{inst}}\eta_e = 0.01$, $\beta_{\text{core}} = 10^{-4}$ and $B = 10 \mu\text{G}$. Line types are the same as in fig. 1. The error-bar represents INTEGRAL’s measurement. According to our model, the flux is dominated by IC emission of accretion shock electrons, and INTEGRAL’s measurement implies $0.06 < \langle f_{\text{inst}} \rangle_{1.3^\circ} \eta_e < 0.23$. The HXR excess measured by INTEGRAL can not be due to secondary emission, since $\beta_{\text{core}} \sim 5$ would be required in order to reproduce the observed flux by secondary emission, implying that the CR energy density is much greater than the thermal energy density of the ICM.

4.2. EGRET’s γ -ray observations

Reimer et al. (2003) report EGRET upper limits on high-energy γ -ray emission from the Coma cluster. EGRET’s upper limit for the flux above 100 MeV is $F_{\text{Coma}} < 3.81 \cdot 10^{-8} \text{ ph cm}^{-2} \text{ s}^{-1}$ (with Coma assumed to be a point source; EGRET’s FWHM at this energy is 5.8°). In fig. 6 we compare the estimated γ -ray flux within a disk of angular radius θ as function of θ for the Coma cluster with an energy threshold of 100 MeV, assuming $f_{\text{inst}}\eta_e = 0.01$, $\beta_{\text{core}} = 10^{-4}$ and $B = 10 \mu\text{G}$, with EGRET’s upper limit. Since the flux is dominated in this band, according to our model, by IC emission of accretion shock electrons, EGRET’s upper limit sets an upper bound for $\eta_e f_{\text{inst}}$ (and only a weak constraint on β_{core} ; Note that the π^0 decays contribute significantly only above $\simeq 122 \text{ MeV}$ due to the threshold for pion production).

Using eqs. (27), (28) and (30), and

$$\int_0^{r_{200, \text{Coma}}/r_{c, \text{Coma}}} (1 + \bar{r}^2)^{-3\beta_{\text{Coma}} + 1/2} \bar{r} d\bar{r} \simeq 0.95, \quad (34)$$

we have

$$F_{\text{Coma, total}} \simeq 7.0 \cdot 10^{-11} \beta_{\text{core}, -4} + 3.0 \cdot 10^{-8} (\langle f_{\text{inst}} \rangle_{1.3^\circ} \eta_e)_{-2} \frac{\text{ph}}{\text{cm}^2 \text{ s}} \quad (35)$$

(since the energy band is close to the pion production threshold, we used the more detailed spectral dependence of the secondaries, as described in § 2.5, to obtain $F_{\text{Coma, pp}} \simeq 7.0 \cdot 10^{-11} \beta_{\text{core}, -4} \text{ ph cm}^{-2} \text{ s}^{-1}$ instead of $F_{\text{Coma, pp}} \simeq 2.0 \cdot 10^{-10} \beta_{\text{core}, -4} \text{ ph cm}^{-2} \text{ s}^{-1}$). EGRET’s upper limit implies therefore $\beta_{\text{core}} < 0.05$ and $\langle f_{\text{inst}} \rangle_{1.3^\circ} \eta_e < 1.4 \cdot 10^{-2}$. We don’t regard the upper limit on $f_{\text{inst}}\eta_e$ to be in contradiction with the range calibrated in § 4.1, since it may be explained by a spatial dependence of f_{inst} , or by a primary electron energy

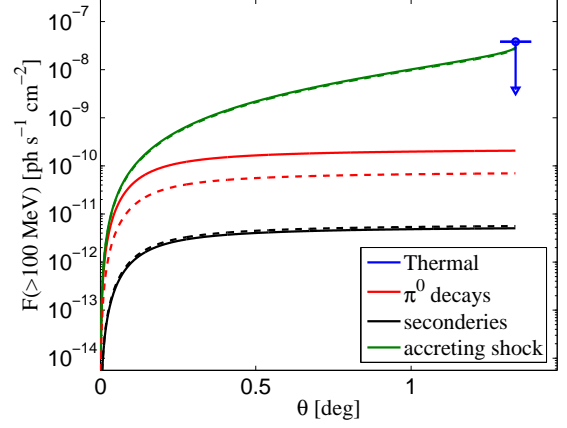


FIG. 6.— The predicted $> 100 \text{ MeV}$ γ -ray flux within a disk of angular radius θ as function of θ for the Coma cluster, assuming $f_{\text{inst}}\eta_e = 0.01$, $\beta_{\text{core}} = 10^{-4}$ and $B = 10 \mu\text{G}$. Line types are the same as in fig. 1. The arrow represents EGRET’s upper limit. The upper limit implies $\langle f_{\text{inst}} \rangle_{1.3^\circ} \eta_e < 1.4 \cdot 10^{-2}$ and $\beta_{\text{core}} < 0.05$.

distribution slightly steeper than $dn/d\varepsilon \propto \varepsilon^{-2}$. Future measurements of the γ -ray emission will thus allow one to constrain the primary electron spectral index.

4.3. VHE γ -ray observations

The Coma cluster has been observed in the VHE γ -ray band with HESS (Domainko et al. 2007) and with VERITAS (Perkins 2008). Both observation are consistent, and we focus on the HESS core observations, which provide more stringent constraints on our model. The upper limit inferred from HESS observations on the flux above 1 TeV within 0.2° is $F_{\text{Coma}} < 8.3 \cdot 10^{-13} \text{ ph cm}^{-2} \text{ s}^{-1}$. In fig. 7 we compare HESS’s upper limit for the Coma cluster with the model predicted $> 1 \text{ TeV}$ γ -ray flux (within a disk of angular radius θ as function of θ), assuming $f_{\text{inst}}\eta_e = 0.01$, $\beta_{\text{core}} = 10^{-4}$ and $B = 10 \mu\text{G}$. Since the energy threshold for this measurement is very high, it provides robust constraints only on β_{core} , through the predicted π^0 decay luminosity. Only weak constraints on $f_{\text{inst}}\eta_e$ may be obtained, due to the uncertainty in the maximal energy to which primary electrons may be accelerated, which is $\sim \text{few TeV}$.

Using eqs. (27), (28) and (30), and

$$\int_0^{0.2^\circ/0.14^\circ} (1 + \bar{r}^2)^{-3\beta_{\text{Coma}} + 1/2} \bar{r} d\bar{r} \simeq 0.43, \quad (36)$$

we have

$$F_{\text{Coma, total}} \simeq 6.8 \cdot 10^{-15} \beta_{\text{core}, -4} + 2.0 \cdot 10^{-14} (\langle f_{\text{inst}} \rangle_{0.2^\circ} \eta_e)_{-2} \frac{\text{ph}}{\text{cm}^2 \text{ s}} \quad (37)$$

(due to the strong dependence of the IC flux on the maximal energy of the primary electrons, we used the exact formulae for IC emission spectra, as described in § 2.5). The upper limit of HESS therefore implies $\beta_{\text{core}} < 1.2 \cdot 10^{-2}$ (and $\langle f_{\text{inst}} \rangle_{0.2^\circ} \eta_e < 0.42$, with large uncertainty).

4.4. Radio observations

In fig. 8 we compare the Thierbach et al. (2003) compilation of flux density measurements of the Coma radio

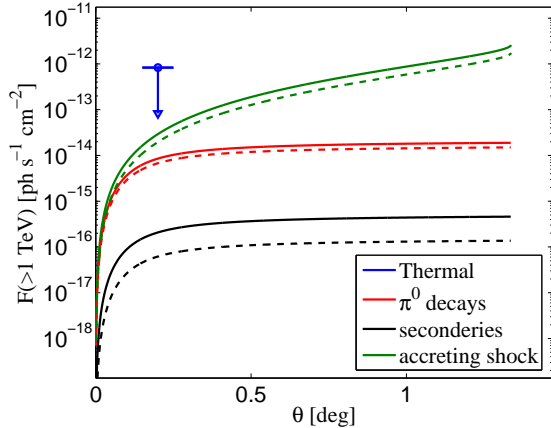


FIG. 7.— The predicted > 1 TeV γ -ray flux within a disk of angular radius θ as function of θ for the Coma cluster, assuming $f_{\text{inst}}\eta_e = 0.01$, $\beta_{\text{core}} = 10^{-4}$ and $B = 10 \mu\text{G}$. Line types are the same as in fig. 1. The arrow represents the upper limit reported by HESS (Domainko et al. 2007), which implies $\beta_{\text{core}} < 1.2 \cdot 10^{-2}$. Only weak constraints on $f_{\text{inst}}\eta_e$ may be obtained, due to the uncertainty in the maximal energy to which primary electrons may be accelerated, which is $\sim \text{few TeV}$.

halo with our model predictions, assuming $B \gg B_{\text{CMB}}$, $\beta_{\text{core}} = 2 \cdot 10^{-4}$, and that the radio halo flux is dominated by synchrotron emission from the secondaries. We note that the spectral steepening observed above $\simeq 2$ GHz is not robust, since it is the result of the subtraction of two big numbers, the total flux and the flux of point sources, and the flux of point sources is not measured but rather extrapolated from lower frequencies assuming a constant spectral index. Since a steepening of the spectra is visible in other sources (for example, the two central galaxies of Coma: NGC4869 and NGC4874), by assuming a constant spectral index one overestimates the point source flux and underestimates the flux density of the diffuse component (Thierbach et al. 2003). Moreover, somewhat above $\simeq 3$ GHz the observed flux is suppressed also by the SZ effect (see Enßlin 2002, for a detailed discussion).

Using eq. (34) and eq. (29) we have

$$\nu S_{\nu, \text{Coma}} \simeq 5.7 \cdot 10^{-1} \beta_{\text{core}, -4} \text{ Jy GHz}. \quad (38)$$

Comparing with observations (see fig. 8) this implies $\beta_{\text{core}} \simeq 2 \cdot 10^{-4}$. Note, that this constraint is consistent with the average value of $\beta_{\text{core}} \simeq 10^{-4}$ derived by Kushnir et al. (2009) for a complete sample of radio emitting galaxy clusters.

5. ICM AND CR EVOLUTION

In § 2 we derived the spectral and radial distribution of the nonthermal emission produced by ICM CRs for massive clusters, $M \gtrsim 10^{14.5} M_{\odot}$. We assumed that the fraction β_{core} of plasma energy carried by CR protons at the central regions of clusters, which dominate the emission from secondary particles, is nearly independent of cluster mass and that the scatter around its average value is small. We have argued, based on simple arguments and crude approximations, that $\beta_{\text{core}} \simeq \eta_p/100$. In what follows we present a simple model for the thermal history of the ICM, including the effects of mergers, which allows us to obtain a more accurate estimate of the value

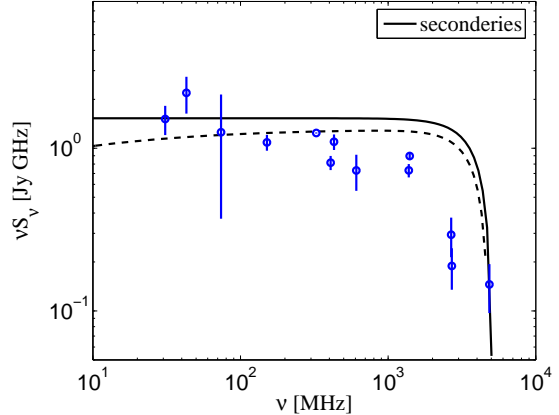


FIG. 8.— A comparison of the Thierbach et al. (2003) compilation of flux density measurements of the Coma radio halo with our model predictions, assuming $B \gg B_{\text{CMB}}$, $\beta_{\text{core}} = 2 \cdot 10^{-4}$, and that the radio halo flux is dominated by synchrotron emission from the secondaries (and taking into account the SZ effect). The spectral steepening observed above $\simeq 2$ GHz is not robust (see text). Line types are the same as in fig. 1.

of $\beta_{\text{CR}, p}$, its spatial dependence within clusters, and its scatter among different clusters.

We first describe in § 5.1 our model for the accretion and merger history of clusters. In § 5.2 a simple model describing the effects of mergers is constructed. The results of § 5.1 and § 5.2 are used in § 5.3 to construct a model for the evolution of CRs in the ICM. The effects of entropy changes that are not driven by gravity (i.e. not due to accretion and merger shocks) are discussed in § 5.4. We assume throughout the analysis that the CR pressure is small compared to the thermal plasma pressure (as supported by observations, see Kushnir et al. 2009).

5.1. Merger and accretion history

We define cluster mass as the mass contained within a radius r_{200} , within which the mean density is 200 times the critical density, $M_{200, z} \equiv M(r_{200}) = (4/3)\pi r_{200}^3 \times 200\rho_{\text{crit}}(z)$. We investigate the present, $z = 0$, non-thermal emission of $M_{200, 0} > 10^{14.5} M_{\odot}$ clusters. For each value of $M_{200, 0}$, chosen from a grid of masses within this range, we construct an ensemble of "merger trees" using the Press & Schechter (1974) based scheme of Lacey & Cole (1993). In order to incorporate the accretion process into this scheme, we assume that merger events involving masses lower than a certain "resolution", M_l , are accretion events. Since the mass accretion rate, \dot{M} , calculated in this manner diverges within the scheme of Lacey & Cole (1993) as the time step tends to zero, we calculate \dot{M} within the frame work of Press-Schechter theory (see § B for details). Figure 9 shows \dot{M} obtained in our scheme for different values of $f_{\text{acc}} \equiv M_l/M_{200, 0}$, normalized to $M_{200, z}/t_{H, z}$, where $t_{H, z}$ is the Hubble time at redshift z . The accretion rate is averaged over 100 realizations of a $M_{200, 0} = 10^{15} M_{\odot}$ cluster. The figure illustrates that \dot{M} depends weakly on the value of f_{acc} , and is lower than $M_{200, z}/t_{H, z}$ at low redshifts by a factor of 2 – 5 for mass resolutions which are adequate for a description of a merger tree (i.e. that reproduce the general results of the Press-Schechter theory). The de-

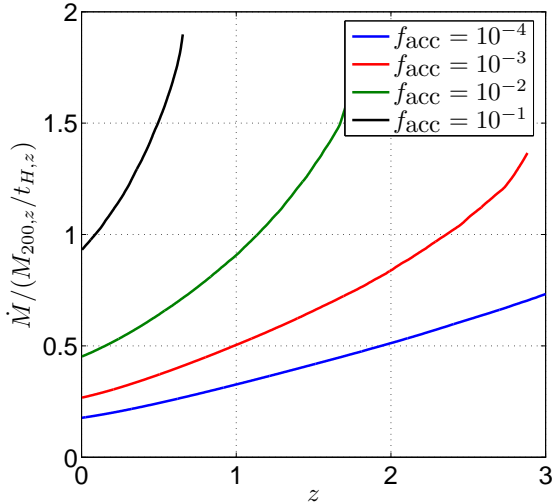


FIG. 9.— Our estimate for the accretion rate, normalized to $M_{200,z}/t_{H,z}$, for different ratios $f_{\text{acc}} \equiv \dot{M}_l/M_{200,0}$. The accretion rate is averaged over 100 realizations of a $M_{200,0} = 10^{15} M_{\odot}$ cluster.

variation of \dot{M} from $M_{200,z}/t_{H,z}$ is expressed in terms of $f_{\text{inst}} \equiv \dot{M}t_{H,z}/M_{200,z}$. As discussed in § 3, 3D numerical simulations indicate that the average value of f_{inst} is ≈ 0.5 at low z . We therefore choose $\dot{M}_l = 2 \cdot 10^{-3} M_{200,0}$, which yields $f_{\text{inst}} \sim 0.5$ for $z < 1$ and $0.5 < f_{\text{inst}} < 1$ for $1 < z < 2.5$. Our results depend only weakly on the value of f_{acc} , and are little modified when $f_{\text{acc}} = 5 \cdot 10^{-4}$ is chosen instead of $f_{\text{acc}} = 2 \cdot 10^{-3}$.

Next we describe how the gas profile is evolved with the addition of accreted mass. We assume that the halos are described, both before and after the accretion, by an NFW density profile (Navarro et al. 1997),

$$\rho(r) = \frac{\rho_s}{(r/r_s)(1+r/r_s)^2}, \quad (39)$$

where $\rho_s = M_s/(4\pi r_s^3)$ and

$$M_s = \frac{M_{200}}{\ln(1+r_{200}/r_s) - (r_{200}/r_s)/(1+r_{200}/r_s)}. \quad (40)$$

r_s is often expressed in terms of the “concentration parameter”, $c_{200} \equiv r_{200}/r_s$. We adopt $c_{200} = 4$ for all of our systems, a value typical of galaxy clusters simulated in a Λ CDM concordance cosmology. Numerous studies (e.g. Eke et al. 2001) found that the mass dependence of the concentration parameter is weak, varying between different clusters by only a factor of ~ 2 .

We assume that the baryon density is proportional to the total (baryon and dark matter) density, $\rho_{\text{gas}} \approx f_b \rho$, where f_b is the cosmic baryon fraction, in agreement with numerical simulations and observations (Borgani et al. 2004; Kravtsov et al. 2005; Vikhlinin et al. 2006). This assumption is not valid within cluster cores, where the gas density profile is flatter than that of the dark matter. Furthermore, the NFW profile is different than the β -model we used for the gas density in § 2. However, the choice of an NFW or a β -model for the gas density is expected to have only a small effect on the inferred value of β_{core} , due to the following reason. As we show below, the production of CR protons is dominated by accretion

shocks and the evolution of their energy density is affected mainly by adiabatic compression. This, combined with the fact that both the NFW and the β -model density profiles imply a ratio of ~ 100 between the gas density in the region that dominates the secondary emission and the gas density at r_{200} , imply that the modification of β_{core} due to the difference between the profiles of such models is small.

Another inaccuracy introduced by using an NFW gas profile is an exaggerated cooling of CR protons in the very center of clusters due to the over estimate of gas density (see eq. (3)). This, however, has only a minor effect on our results since the cooling affects only a small fraction of the gas mass (see § 5.3). We chose to work with an NFW density profile despite the above limitations, since it allows us to derive a very simple model for the description of cluster mergers (see § 5.2).

In order to completely specify the properties of the gas, we must choose an entropy profile. Assuming hydrostatic equilibrium,

$$\frac{dp(r)}{dr} = -\frac{GM(r)}{r^2} \rho_{\text{gas}}(r), \quad (41)$$

the entropy is deduced from the equation of state, $p = K \rho_{\text{gas}}^{5/3}$. A boundary condition must be specified for eq. (41). We choose to specify a value for the pressure of the gas at r_{200} . Although there is some freedom in the choice of the pressure at r_{200} , the entropy profile is rather insensitive to $p(r=r_{200})$ (for physically reasonable values, see McCarthy et al. 2007). Since at intermediate radii the NFW profile is well approximated by an isothermal profile, i.e. $\rho \propto r^{-2}$ and $d \ln K / d \ln M_{\text{gas}} = 4/3$, we choose a value of $p(r_{200})$ that establishes this near pure power-law entropy distribution all the way out to r_{200} . Voit et al. (2002) have demonstrated that groups and clusters are indeed expected to have near power-law entropy distributions out to large radii.

Assuming that a hydrostatic NFW profile is preserved in the accretion process, we modify, following accretion, the density and the temperature of each mass element according to its Lagrangian location, in order to match the post-accretion hydrostatic NFW profile. We finally assume that the accreted mass was shocked at an infinite Mach number shock to the density and temperature at the outskirts of the post-accretion hydrostatic NFW profile.

5.2. A simple model for mergers

Let us next construct a simple model describing the evolution of ICM gas in merger events. We first note that the most frequent mergers occur between halos of similar mass. This is illustrated in fig. 10, which shows the distribution of the ratio between the primary (heavier halo) mass, M_p , and secondary (lighter halo) mass, M_s , over 100 runs for $M_{200,0} = 10^{15} M_{\odot}$. The distribution is weighted by the secondary mass, since the thermodynamic variables of the secondary halo are more affected in merger events than the primary ones. According to fig. 10, high mass ratio mergers, $M_p/M_s > 10$, are rare. We therefore treat such mergers in a very approximated manner, as described below. Note, that although the mass accumulated in high mass ratio mergers is a small fraction of the total cluster mass, it is not necessarily small compared to the cluster core mass, which

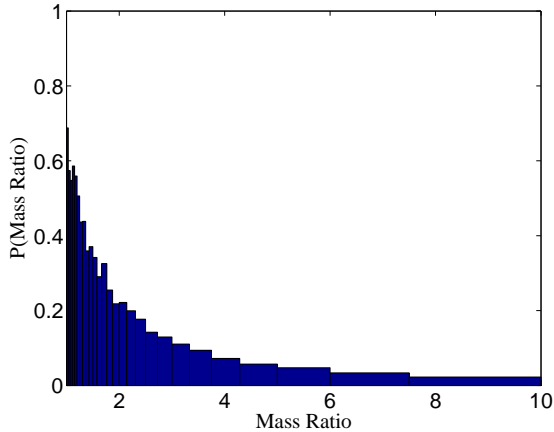


FIG. 10.— The distribution of primary to secondary halo mass ratio in mergers, obtained from 100 realizations of the merger history for $M_{200,0} = 10^{15} M_{\odot}$. The distribution is weighted by the secondary mass, since the thermodynamic variables of the secondary halo are more affected in merger events than the primary ones.

dominates the secondary emission. Thus, high mass ratio mergers could have affected the nonthermal emission, had the mass of the secondary accreted halos been accumulated in the cluster core. Numerical simulations (e.g. McCarthy et al. 2007) indicate that this is not the case: For $M_p/M_s = 10$ the secondary halo penetrates through the massive one and its mass is spread, on a Hubble time scale, over the entire primary halo.

For the description of small mass ratio mergers we rely on detailed 3D numerical simulations (e.g. McCarthy et al. 2007). We assume that the halos are described, both before and after mergers, by an NFW density profile. We show that this assumption, combined with the inference from numerical simulations that during the merger the ICM is shocked twice (with the two shocks separated by adiabatic expansion), completely determines the Mach numbers of the shocks and the magnitude of the adiabatic expansion experienced by different fluid elements.

We assume that the available energy to be thermalized in the merger is divided equally between the two shock episodes. This determines the Mach number of each mass element in each shock episode (for details, see McCarthy et al. 2007), such that the only two free parameters are the magnitudes of the adiabatic expansion experienced by each cluster. Assuming that the profile of the merged cluster is produced by sorting the gas elements of the initial clusters according to their density, the two adiabatic expansion factors are determined by minimizing the difference between the resulting profile and a hydrostatic NFW profile. In order to illustrate the procedure used, fig. 11 and fig. 12 show the resulting density and entropy profiles for a merger with a 1 : 1 mass ratio. Merging the clusters, and sorting according to density leads to an exact NFW profile, with entropy which is lower than required by hydrostatic equilibrium. After the first shock, the entropy becomes higher but the resulting density exceeds the NFW density. Adiabatic expansion and a second shock then lead to density and entropy profiles which are very close to NFW at hydrostatic equilibrium. The expansion factor required for obtaining the required final NFW density and entropy is

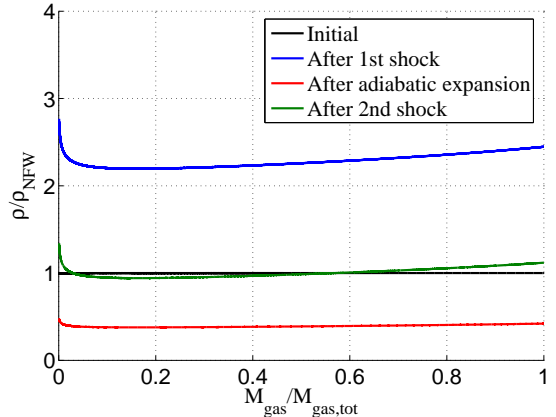


FIG. 11.— The gas density of the merged cluster as function of the accumulated gas mass for an equal mass merger, for a calibrated adiabatic expansion density decrease factor (see text) of $\simeq 0.17$. The profile of the merged cluster is produced by sorting the gas elements of the initial clusters according to their density.

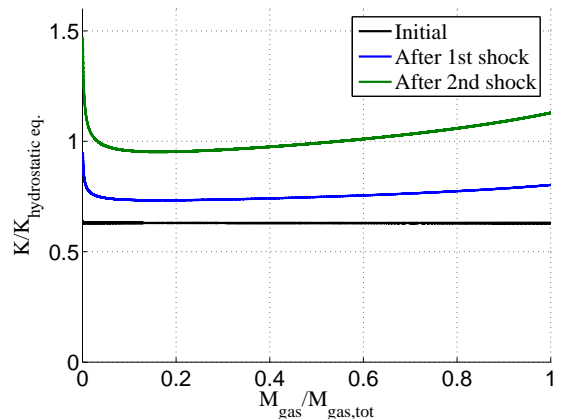


FIG. 12.— Same as fig. 11 for the entropy of the merged cluster gas.

$\simeq 6$, corresponding to a density decrease factor of $\simeq 0.17$

It is remarkable that this simple model reproduces a post-merger hydrostatic NFW halo. We note that assuming a different density profile for the halo (for example, a β -model, see § 2) does not allow one to preserve the density profile in the post merger cluster using such a simple model. The density decrease factors determined by this method for mergers of different mass ratios are shown in fig. 13. Above a mass ratio of 10 : 1 we simply sort the gas elements according to their density, and change the density and the temperature of each mass element according to its Lagrangian location, in order to reproduce the post-merger hydrostatic NFW profile. The details of large mass ratio mergers have only a small effect on our results.

One of the results of our model is the merger shocks' Mach number distribution. We show this distribution, weighted by the mass of the shocked gas, in fig. 14, based on 100 merger history realizations for a cluster with $M_{200,0} = 10^{15} M_{\odot}$ (the first bin is not shown, since almost all of the shocks are included in it). As can be seen from the figure, the maximal Mach number achieved in merger shocks is smaller than 2.5, in agreement with the numerical simulations of Skillman et al. (2008). Since

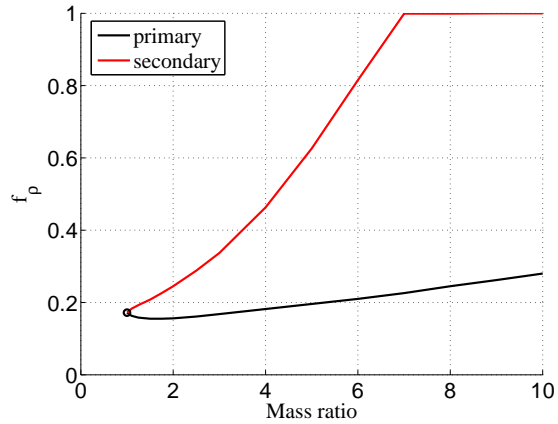


FIG. 13.— Calibrated adiabatic expansion factors as function of merging clusters mass ratio.

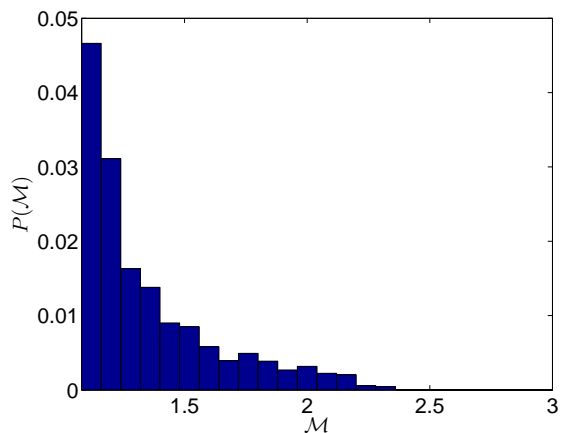


FIG. 14.— Merger shocks' Mach number distribution, weighted by the mass of the shocked gas, averaged over 100 merger history realizations, for a cluster with $M_{200,0} = 10^{15} M_{\odot}$. The first bin is not shown, since almost all of the shocks are included in it. The maximal Mach number achieved in mergers is smaller than 2.5.

such weak shocks are assumed to produce very steep CR spectra (see § 1), with normalization that depends on poorly known conditions at the injection energy of the CRs, we ignore acceleration in merger shocks hereafter.

5.3. CR evolution

After determining, in § 5.1 and § 5.2, the thermodynamic history of the ICM plasma, we turn now to the evolution of the CR population. We follow here only the evolution of CR protons, since we are only interested in the value of β_{core} . The processes that we include in the calculations are: injection of CRs in accretion shocks (we neglect injection in weak merger shocks, see § 5.2), proton energy losses due to Coulomb and inelastic nuclear collisions, using the parametrization of Kamae et al. (2006) for the p-p interaction, modification of the CR energy density due to adiabatic expansion/compression (assuming the CRs to behave as a relativistic gas with an adiabatic index of 4/3). As explained in the introduction, we assume that CR diffusion is not important, and that the CRs are coupled to the thermal plasma by magnetic fields. We also assume that the CR pressure is small compared to the thermal plasma pressure (as supported by observations, see Kushnir et al. 2009). We calculate

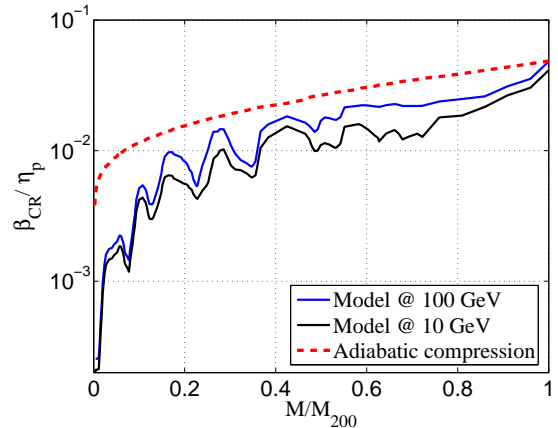


FIG. 15.— β_{CR}/η_p at 100 GeV (blue) and at 10 GeV (black), as function of the accumulated mass for a typical $M_{200,0} = 10^{15} M_{\odot}$ cluster. The red line shows a $\rho_{\text{gas}}^{-1/3}$ scaling of β_{CR}/η_p , normalized at the accretion shock.

numerically the CR content of each mass element in the cluster, following the thermodynamic evolution of this mass element and describing the CR energy distribution using a discrete (Lagrangian, logarithmically spaced) set of energy bins.

Figure 15 presents typical distributions of $\beta_{\text{CR},p}(\varepsilon = 100 \text{ GeV})/\eta_p$ and $\beta_{\text{CR},p}(\varepsilon = 10 \text{ GeV})/\eta_p$, obtained for one realization of the evolution of a $10^{15} M_{\odot}$ cluster. $\beta_{\text{CR},p}$ depends weakly on energy, as demonstrated in the figure, from $\sim 10 \text{ GeV}$ up to the maximal energy to which the CR protons are accelerated. The spatial distribution of $\beta_{\text{CR},p}$ approximately follows $\rho_{\text{gas}}^{-1/3}$, with normalization fixed at the accretion shock. $\beta_{\text{CR},p}$ falls somewhat below this scaling at the cluster center mainly due to the effect of weak shocks (which lead to compression without significant production of high energy CRs) and due to proton energy loss at the high density cluster core. The latter effect is exaggerated in our calculations due to our assumption that the gas density follows the dark matter density. However, cooling affects only a small fraction (1%) of the gas mass. The fact that $\beta_{\text{CR},p}$ follows approximately $\rho_{\text{gas}}^{-1/3}$ implies that its evolution is determined mainly by the adiabatic compression of the ICM plasma, and that mergers do not significantly modify $\beta_{\text{CR},p}$.

We define β_{core} as the mass average of β_{CR} at 100 GeV within the inner 10% of the cluster mass, which corresponds to the core region. Figure 16 shows the average value and the scatter of $\beta_{\text{core}}/\eta_p$ as function of the cluster mass at $z = 0$. As can be seen from the figure, $\beta_{\text{core}}/\eta_p \simeq 1/200$ is a good approximation for $M_{200,0} > 10^{14.5} M_{\odot}$. β_{core} depends only weakly on cluster mass, changing by a factor of less than 2 over one decade of cluster mass, with a factor ~ 2 scatter between different clusters of given mass.

5.4. The effects of "non-gravitational" entropy changes

Our model for the ICM evolution takes into account entropy changes of the ICM driven by gravity only (accretion and merger shocks), and assumes that the galaxy clusters' density and entropy profiles are self-similar. It is

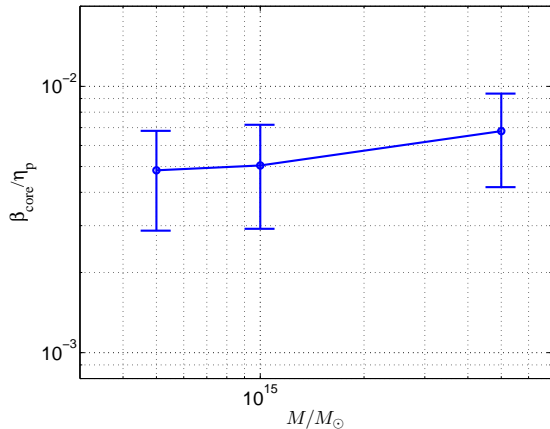


FIG. 16.— β_{core} (the mass average of $\beta_{\text{CR},p}$ at 100 GeV within the inner 10% of the cluster mass) as function of cluster mass at $z = 0$. The average value (for a given cluster mass) was obtained from 100 realizations of merger histories, and the error bar represents the 1σ scatter of the $\beta_{\text{CR},p}$ distribution.

well known (see e.g. Arnaud & Evrard 1999) that models taking into account only gravitational effects and assuming self-similarity lead to a correlation $L_X \propto T^2$ between the bolometric X-ray luminosity, L_X , and the temperature of the clusters, T , which is flatter than the observed correlation, $L_X \propto T^{2.5}$ (see, e.g. Reiprich & Bohringer 2002). This deviation from self-similarity is commonly explained as due to entropy increase of the gas at some high redshift by non-gravitational processes such as supernovae, star formation and galactic winds (e.g. Kaiser 1991; Evrard & Henry 1991; Navarro et al. 1995; Cavaliere et al. 1997; Balogh et al. 1999; Ponman et al. 1999). Although such entropy increase does not modify significantly the entropy profile of the massive clusters in which we are interested, one may worry about its possible effect on the CR population, since part of the gas residing in high mass clusters has, in the past, been associated with low mass clusters. The CR energy density in low mass clusters may be reduced by an early entropy increase, which reduces the Mach numbers of accretion shocks. Repeating our calculations including an early entropy increase we find, however, that this effect is rather small. Early (non-gravitational) entropy increase may reduce the Mach numbers of accretion shocks to values which significantly affect CR production only for clusters of mass $< 10^{13} M_{\odot}$, and the suppression of CR production in such shocks reduces the value of β_{core} in massive clusters by no more than 20%.

Another non-gravitational effect that may modify the ICM entropy is radiative cooling at the cores of massive clusters. This effect may lead to an increase of the ratio of CR to thermal ICM energy density and may therefore affect the predicted secondary emission. However, numerical simulations (Pfrommer et al. 2007) predict that the effect of cooling on the nonthermal secondary emission is not very large, as can be estimated by examining the simulated γ -ray emission from massive clusters, for radiative and non-radiative simulations. This is probably due to the fact that cooling affects mainly the inner few tens of kpc, while the secondary emission is dominated by a larger region, ~ 300 kpc. We note that it is well-known that the effects of cooling flows are exag-

gerated in numerical simulations (e.g. Balogh et al. 2001; Borgani et al. 2004, 2006, and references therein).

6. DISCUSSION

We have derived analytic expressions, eqs. (9)–(26), which approximately describe the spectral and radial distribution of the nonthermal emission produced by (primary and secondary) CRs in massive, $M \gtrsim 10^{14.5} M_{\odot}$, galaxy clusters. These expressions depend on the (observed) cluster thermal X-ray properties and on two model parameters, β_{core} and η_e . We have shown (see § 5) that CR production is dominated by strong accretion shocks, and that the energy density of CR protons is mainly affected (after production) by the adiabatic compression of the ICM plasma. Simple arguments based on crude approximations imply that adiabatic compression should lead to $\beta_{\text{core}} \sim \eta_p/100$ (§ 2, see also Pfrommer et al. 2007; Jubelgas et al. 2008). A more detailed analysis of the thermodynamic history of the ICM (§ 5) yields $\beta_{\text{core}} \simeq \eta_p/200$, nearly independent of cluster mass and with a scatter $\Delta \ln \beta_{\text{core}} \simeq 1$ between clusters of given mass (see fig. 16). The analysis presented in § 5 includes a simple description of the thermodynamic history of the ICM, as determined by merger and accretion events, and a calculation of the energy and spatial distribution of CR protons. We have shown in § 4 that our model’s results agree with those of detailed numerical calculations, and that discrepancies between the results of various numerical simulations (and between such results and our model) are due to inaccuracies in the numerical calculations.

The charged secondary emission depends on the strength of the magnetic field in the cluster core. It is given in § 2.3 in terms of B/B_{CMB} , the ratio of the magnetic field to B_{CMB} , defined as the magnetic field for which the magnetic energy density equals the CMB energy density, $B_{\text{CMB}} \simeq 3 \mu\text{G}$. Since the secondary e^{\pm} emission is dominated at high energy, $\gtrsim 1$ eV, by secondary π^0 decay and by IC emission of primary electrons, the uncertainty in the value of B affects only the predicted radio emission, which is not the main focus of the current paper. The detailed discussion of radio emission from clusters given in Kushnir et al. (2009) indicates that B is within the range of $\sim 1 \mu\text{G}$ to $\sim 10 \mu\text{G}$.

Our model predicts that the HXR and γ -ray luminosities produced by IC scattering of CMB photons by electrons accelerated in accretion shocks exceed the luminosities produced by secondary particles by factors $\simeq 500(\eta_e/\eta_p)(T/10\text{keV})^{-1/2}$ and $\simeq 150(\eta_e/\eta_p)(T/10\text{keV})^{-1/2}$ respectively, where T is the cluster temperature. Secondary particle emission may dominate at the radio and VHE ($\gtrsim 1$ TeV) γ -ray bands. Our model predicts, in contrast with some earlier work that neglected the primary IC emission, that the HXR and γ -ray emission from clusters of galaxies are extended, since the emission is dominated at these energies by primary (rather than by secondary) electrons. Our model is supported by observations of the Coma cluster, where the HXR image does not show any significant substructure, the measured HXR flux corresponds to a reasonable efficiency of electron acceleration, $\eta_e \sim$ a few percent, and the radio emission corresponds to a reasonable efficiency of proton acceleration, $\beta_{\text{core}} \sim 10^{-4}$ implying $\eta_p \sim$ a few percent (see § 4). As explained in § 4.1 (see also

Kushnir et al. 2009), in order for secondary emission to reproduce the HXR emission of Coma, an unreasonably high CR energy density is required.

We have assumed in our analysis that the ICM plasma is isothermal and in hydrostatic equilibrium. Deviations from this simple model near the virial radius may change our estimates for $\eta_{e,p}$. Although such deviations are only weakly constrained by observations, both observational (e.g. Vikhlinin et al. 2005) and theoretical (e.g. Roncarelli et al. 2006) analyses indicated that they are not large (for example, the accretion shock temperature is lower than the virial temperature by no more than a factor ~ 2). Modifications of the ICM properties near the virial radius may be easily incorporated into our model. Improved (observational) determination of the ICM profile near the virial radius will therefore allow one to improve the accuracy of the determination of $\eta_{e,p}$.

Our model predicts, that future HXR observations (e.g. NuStar, Simbol-X) and space-based γ -ray observations (Fermi) will lead to detection of clusters of galaxies as extended sources. Since EGRET's sensitivity is marginally too low for such detection (see § 4), we predict Fermi's ~ 50 times better sensitivity would suffice. Single sources could be detected and resolved in both energy bands (the angular resolution of Fermi can be as low as 0.1° and that of future HXR observation may reach tens of arcsec). We give in table 1 the predicted flux above 50 GeV within 0.1° for the 10 most luminous clusters from the extended sample of Reiprich & Bohringer (2002), assuming $\eta_e f_{\text{inst}} = 0.01$. We also give the cluster angular radius. For cluster diameters larger than 0.2° it would be possible to distinguish between extended and core emission with Fermi, thus discriminating between secondary emission from the core and primary emission from the accretion shock.

Figure 7 shows that the current upper limit on the VHE γ -ray flux from the core of the Coma cluster is higher than the predicted flux by a factor of ~ 100 . This implies that a detection of the predicted Coma core flux is not possible with current generation imaging Cerenkov telescopes. Imaging telescopes may, however, allow us to detect the predicted high energy emission produced by the accretion shock. It should be pointed out that lowering the threshold energy of the imaging Cerenkov telescopes to ~ 0.1 TeV is important for this type of observation, since there is a large uncertainty in the predicted flux at energies > 1 TeV, due to the uncertainty in the exact value of the maximal energy to which electrons

can be accelerated, which is \sim few TeV. The sources in table 1 are also optimal for imaging telescopes.

In order to detect pion decay emission from cluster cores, two approaches may be adopted. One may construct high resolution ($\sim 0.1^\circ$) HXR maps and compare them to the γ -ray maps. Since the correlation between the HXR and the γ -ray maps should be due to the primary IC emission from the accretion shock, their difference should trace the pion decay contribution. Alternatively, one may identify clusters which may be resolved and for which the surface brightness of the core is dominated by pion decays, so that a sharp decrease in the surface brightness with radius may be observed. Table 2 gives a list of the best candidates for such detection: The predicted flux above 50 GeV within 0.1° is given for the 10 clusters with the highest pion to IC ratio from the extended sample of Reiprich & Bohringer (2002), assuming $\eta_e f_{\text{inst}} = 0.01$ and $\beta_{\text{core}} = 10^{-4}$. We considered only clusters with angular radius exceeding 0.2° , which may be resolved.

As illustrated by the analysis of the observations of the Coma cluster, high energy and radio observations of a controlled sample of clusters will allow one to calibrate the model parameters $\eta_e f_{\text{inst}}$ and β_{core} . Determination of f_{inst} and $\beta_{\text{core}}/\eta_p$ from numerical simulations would then allow one to determine η_p and η_e . Analysis of cluster radio emission, leading to a determination of β_{core} and of the strength of magnetic fields in cluster cores, is reported by Kushnir et al. (2009). Analysis of all clusters observed in HXR, aimed at determining $\eta_e f_{\text{inst}}$, is reported by Kushnir & Waxman (2010). Since the group of clusters observed in HXR is not a complete controlled sample, the determination of $\eta_e f_{\text{inst}}$ based on current observations may be biased. A controlled sample may be produced by future HXR observations (e.g. NuStar, Simbol-X). Moreover, such missions may produce high resolution HXR maps of clusters, testing the prediction that the emission is extended, i.e. originating from the accretion shock. Finally, we note that measurements of the nonthermal emission in different bands (e.g. HXR and γ -rays for electrons, radio and VHE γ -rays for protons) would allow one to constrain the energy distribution of the accelerated particles.

We thank C. Pfrommer for useful discussions. This research was partially supported by ISF, Minerva and AEC grants.

APPENDIX

A. EMISSION MECHANISMS

Thermal emission

The bolometric bremsstrahlung emissivity at some radius is given by

$$\epsilon_X(r) \simeq \sqrt{\frac{8}{3\pi}} \sigma_T \alpha_e c \sqrt{m_e c^2} T^{1/2} m_p^{-2} \mu_e^{-1} \left(\frac{1}{\mu_H} + \frac{4}{\mu_{\text{He}}} \right) \rho_{\text{gas}}^2(r), \quad (\text{A1})$$

(assuming the thermal Gaunt factor to be 1 and neglecting elements heavier than Helium, which may increase the bremsstrahlung emissivity by a few tens of percent). Here α_e is the fine structure constant and we use the definitions $n_e = \rho_{\text{gas}}/(\mu_e m_p)$, $n_H = \rho_{\text{gas}}/(\mu_H m_p)$ and $n_{\text{He}} = \rho_{\text{gas}}/(\mu_{\text{He}} m_p)$ for the electron, Hydrogen and Helium number densities, respectively (which yield $\mu_e \simeq 1.14$, $\mu_H \simeq 1.33$ and $\mu_{\text{He}} \simeq 16$ for fully ionized gas with hydrogen mass fraction $\chi = 0.75$).

TABLE 1. THE PREDICTED IC FLUX ABOVE 50 GeV WITHIN 0.1° FOR THE 10 MOST LUMINOUS CLUSTERS FROM THE EXTENDED SAMPLE OF REIPRICH & BOHRINGER (2002), ASSUMING $\eta_e f_{inst} = 0.01$.

Cluster name	Flux [10^{-12} ph cm $^{-2}$ s $^{-1}$]	Angular radius [deg]
A2163	0.71	0.21
A1914	0.45	0.22
Ophiuchus	0.40	1.3
A3888	0.38	0.25
A0754	0.34	0.65
A1689	0.33	0.18
Triangulum	0.31	0.63
A2142	0.31	0.35
A3266	0.27	0.56
A2029	0.27	0.40

TABLE 2. THE PREDICTED FLUX ABOVE 50 GeV WITHIN 0.1° FOR THE 10 CLUSTERS WITH THE HIGHEST PION TO IC RATIO FROM THE EXTENDED SAMPLE OF REIPRICH & BOHRINGER (2002), ASSUMING $\eta_e f_{inst} = 0.01$ AND $\beta_{core} = 10^{-4}$.

Cluster name	Pion decays flux [10^{-13} ph cm $^{-2}$ s $^{-1}$]	IC flux [10^{-12} ph cm $^{-2}$ s $^{-1}$]	ratio	Angular radius [deg]
Perseus	3.1	0.15	2.0	1.4
A3526	0.49	0.05	1.0	1.7
NGC 4636	0.026	0.003	0.80	2.2
2A 0335	0.30	0.038	0.79	0.50
NGC 5813	0.017	0.0024	0.73	1.3
Ophiuchus	2.7	0.4	0.67	1.3
A0262	0.12	0.018	0.65	0.80
A2199	0.41	0.072	0.56	0.72
A0496	0.33	0.059	0.56	0.57
NGC 5044	0.034	0.0061	0.56	1.1

Neutral secondaries emission

The p-p γ -ray emissivity per logarithmic photon energy bin, $\nu\epsilon_\nu^{pp}$, due to the decay of neutral pions produced in inelastic nuclear collisions, is given to a very good approximation by (Katz & Waxman 2008)

$$\begin{aligned} \nu\epsilon_\nu^{pp}(r) &\simeq 2f_{pp} \cdot \varepsilon^2 \left(\frac{dn}{d\varepsilon} \right) \cdot 0.1 \frac{\rho_{gas}(r)}{m_p} \left(\frac{1}{\mu_H} + \frac{1}{\mu_{He}} \right) c\sigma_{pp}^{inel} \\ &\simeq 0.2f_{pp} \frac{3}{2} c\beta_{CR} m_p^{-2} \mu^{-1} \left(\frac{1}{\mu_H} + \frac{1}{\mu_{He}} \right) T \rho_{gas}^2(r) \sigma_{pp}^{inel}, \end{aligned} \quad (A2)$$

where $\sigma_{pp}^{inel} \simeq 40$ mb and $f_{pp} \simeq 0.75$. Since the CR protons have flat spectra, $\nu\epsilon_\nu^{pp}$ is not energy dependent at the relevant photon energies, from ~ 0.1 GeV ($\varepsilon_{th} \simeq 1.22$ GeV is the threshold energy for pion production and the photon energy is ~ 0.1 of the proton energy) up to the cutoff energy due to pair production in interaction with the IR background, which should be around ~ 10 TeV for nearby clusters (Franceschini et al. 2008). Using eq. (A1) and eq. (A2), the total p-p γ -ray luminosity, νL_ν^{pp} , is related to the bolometric bremsstrahlung luminosity, L_X , by

$$\begin{aligned} \nu L_\nu^{pp} &\simeq \frac{\mu_e}{\mu} \frac{\frac{1}{\mu_H} + \frac{1}{\mu_{He}}}{\frac{1}{\mu_H} + \frac{4}{\mu_{He}}} \frac{3}{2} \cdot 0.2f_{pp} \sigma_{pp}^{inel} \beta_{CR} T^{1/2} L_X \\ &\simeq 1.3 \cdot 10^{41} \beta_{core,-4} T_1^{1/2} \left(\frac{L_X}{h_{70}^{-2} 3 \cdot 10^{45} \text{ erg s}^{-1}} \right) \text{ erg s}^{-1}. \end{aligned} \quad (A3)$$

Using the correlations eq. (6), we have

$$\nu L_\nu^{pp} \simeq 1.2 \cdot 10^{41} \beta_{core,-4} T_1^{3.06} \text{ erg s}^{-1}. \quad (A4)$$

The p-p γ -ray surface brightness above some energy $\varepsilon_{\nu, \min}$ at some distance $\bar{r} \equiv r/r_c$ from the cluster center is given

by (for $\beta > 0.5$, see Sarazin & Bahcall 1977)

$$\begin{aligned}
S_{\nu > \nu_{\min}}^{\text{PP}}(\bar{r}) &\simeq \frac{1}{2\pi^{5/2}} 0.886 \nu L_{\nu}^{\text{PP}} r_c^{-2} \left(3\beta - \frac{3}{2}\right) (1 + \bar{r}^2)^{-3\beta+1/2} (\max(\varepsilon_{\nu, \min}, 0.1\varepsilon_{\text{th}}))^{-1} \\
&\simeq 5.5 \cdot 10^{-7} \left(3\beta - \frac{3}{2}\right) \beta_{\text{core}, -4} T_1^{1/2} \left(\frac{L_X}{h_{70}^{-2} 3 \cdot 10^{45} \text{ erg s}^{-1}}\right) \left(\frac{r_c}{h_{70}^{-1} 200 \text{ kpc}}\right)^{-2} \\
&\times \left(\frac{\max(\varepsilon_{\nu, \min}, 0.1\varepsilon_{\text{th}})}{10 \text{ GeV}}\right)^{-1} (1 + \bar{r}^2)^{-3\beta+1/2} \text{ ph cm}^{-2} \text{ s}^{-1} \text{ sr}^{-1}
\end{aligned} \tag{A5}$$

(neglecting the $\gamma\gamma \rightarrow e^+e^-$ cutoff). Using the correlations eq. (6) we have

$$S_{\nu > \nu_{\min}}^{\text{PP}}(\bar{r}) \simeq 4.1 \cdot 10^{-7} \left(3\beta - \frac{3}{2}\right) \beta_{\text{core}, -4} T_1^{0.42} \left(\frac{\max(\varepsilon_{\nu, \min}, 0.1\varepsilon_{\text{th}})}{10 \text{ GeV}}\right)^{-1} (1 + \bar{r}^2)^{-3\beta+1/2} \text{ ph cm}^{-2} \text{ s}^{-1} \text{ sr}^{-1}. \tag{A6}$$

IC emission from charged secondaries

p-p collisions also produce secondary electrons and positrons, which cool by emitting synchrotron radiation and by IC scattering of CMB photons. We assume that the distribution of the secondaries is in a steady state, where in the relevant energy bands the secondaries that are generated lose all their energy to radiation. Since the CR protons have flat spectra, the secondary production ($\varepsilon L_{\varepsilon}^{\pm}$) in the range $0.1\varepsilon_{\text{th}} < \varepsilon_{e^{\pm}} < 0.1\varepsilon_{\text{max}}$ is not energy dependent. To a very good approximation, the production in this energy range satisfies

$$\varepsilon L_{\varepsilon}^{\pm} \simeq \frac{f_{e^-} + f_{e^+}}{4} \nu L_{\nu}^{\text{PP}}, \tag{A7}$$

where $f_{e^-} \simeq 0.8$ and $f_{e^+} \simeq 1.2$. As explained in § 2, we consider only secondaries with cooling time shorter than t_{dyn} . For values $1 - 10 \mu\text{G}$ of the magnetic field, the Lorentz factor of secondaries with cooling time which equals the dynamical time is $200 \lesssim \gamma_{\text{cool}} \lesssim 2000$.

To a very good approximation, in the range of photon energies $\gamma_{\text{cool}}^2 3T_{\text{CMB}}(1+z)^4 < \varepsilon_{\text{ph}} < \gamma_{\text{max}}^2 3T_{\text{CMB}}(1+z)^4$, where $\gamma_{\text{max}} \simeq 0.1\varepsilon_{\text{max}}/m_e c^2$ (ε_{max} is the maximal energy of the CR protons and the secondaries energy is ~ 0.1 of the proton energy), the luminosity due to IC scattering from the secondaries is given by

$$\begin{aligned}
\nu L_{\nu}^{\text{IC}, e^{\pm}} &\simeq \frac{1}{2} \varepsilon L_{\varepsilon}^{\pm} \frac{B_{\text{CMB}}^2}{B_{\text{CMB}}^2 + B^2} \simeq \frac{f_{e^+} + f_{e^-}}{8} \nu L_{\nu}^{\text{PP}} \frac{B_{\text{CMB}}^2}{B_{\text{CMB}}^2 + B^2} \\
&\simeq 3.3 \cdot 10^{40} \frac{B_{\text{CMB}}^2}{B_{\text{CMB}}^2 + B^2} \beta_{\text{core}, -4} T_1^{1/2} \left(\frac{L_X}{h_{70}^{-2} 3 \cdot 10^{45} \text{ erg s}^{-1}}\right) \text{ erg s}^{-1},
\end{aligned} \tag{A8}$$

and the surface brightness is given by

$$\begin{aligned}
S_{\nu > \nu_{\min}}^{\text{IC}, e^{\pm}}(\bar{r}) &\simeq \frac{1}{2\pi^{5/2}} 0.886 \nu L_{\nu}^{\text{IC}, e^{\pm}} r_c^{-2} \left(3\beta - \frac{3}{2}\right) (1 + \bar{r}^2)^{-3\beta+1/2} (\varepsilon_{\nu, \min})^{-1} \\
&\simeq 1.4 \cdot 10^{-7} \left(3\beta - \frac{3}{2}\right) \frac{B_{\text{CMB}}^2}{B_{\text{CMB}}^2 + B^2} \beta_{\text{core}, -4} T_1^{1/2} \left(\frac{L_X}{h_{70}^{-2} 3 \cdot 10^{45} \text{ erg s}^{-1}}\right) \left(\frac{r_c}{h_{70}^{-1} 200 \text{ kpc}}\right)^{-2} \\
&\times \left(\frac{\varepsilon_{\nu, \min}}{10 \text{ GeV}}\right)^{-1} (1 + \bar{r}^2)^{-3\beta+1/2} \text{ ph cm}^{-2} \text{ s}^{-1} \text{ sr}^{-1}.
\end{aligned} \tag{A9}$$

Using the correlations eq. (6), we have

$$\nu L_{\nu}^{\text{IC}, e^{\pm}} \simeq 3.0 \cdot 10^{40} \frac{B_{\text{CMB}}^2}{B_{\text{CMB}}^2 + B^2} \beta_{\text{core}, -4} T_1^{3.06} \text{ erg s}^{-1}, \tag{A10}$$

and

$$S_{\nu > \nu_{\min}}^{\text{IC}, e^{\pm}}(\bar{r}) \simeq 1.0 \cdot 10^{-7} \left(3\beta - \frac{3}{2}\right) \frac{B_{\text{CMB}}^2}{B_{\text{CMB}}^2 + B^2} \beta_{\text{core}, -4} T_1^{0.42} \left(\frac{\varepsilon_{\nu, \min}}{10 \text{ GeV}}\right)^{-1} (1 + \bar{r}^2)^{-3\beta+1/2} \text{ ph cm}^{-2} \text{ s}^{-1} \text{ sr}^{-1}. \tag{A11}$$

Synchrotron emission from charged secondaries

To a very good approximation, in the range of photon energies $\gamma_{\text{cool}}^2 \varepsilon_0 < \varepsilon_{\text{ph}} < \gamma_{\text{max}}^2 \varepsilon_0$, where $\varepsilon_0 = 3heB/4\pi m_e c$, the synchrotron luminosity from the secondaries is given by

$$\begin{aligned}
\nu L_{\nu}^{\text{sync}, e^{\pm}} &\simeq \nu L_{\nu}^{\text{IC}, e^{\pm}} \frac{B^2}{B_{\text{CMB}}^2} \\
&\simeq 3.3 \cdot 10^{40} \frac{B^2}{B_{\text{CMB}}^2 + B^2} \beta_{\text{core}, -4} T_1^{1/2} \left(\frac{L_X}{h_{70}^{-2} 3 \cdot 10^{45} \text{ erg s}^{-1}}\right) (1+z)^{-4} \text{ erg s}^{-1}.
\end{aligned} \tag{A12}$$

and the surface brightness is given by:

$$\begin{aligned}
S_{\nu}^{\text{sync},e^{\pm}}(\bar{r}) &\simeq \frac{1}{2\pi^{5/2}} 0.886\nu L_{\nu}^{\text{sync},e^{\pm}} r_c^{-2} \left(3\beta - \frac{3}{2}\right) (1 + \bar{r}^2)^{-3\beta+1/2} \nu^{-1} \\
&\simeq 13 \left(3\beta - \frac{3}{2}\right) \frac{B^2}{B_{\text{CMB}}^2 + B^2} \beta_{\text{core},-4} T_1^{1/2} \left(\frac{L_X}{h_{70}^{-2} 3 \cdot 10^{45} \text{ erg s}^{-1}}\right) \left(\frac{r_c}{h_{70}^{-1} 200 \text{ kpc}}\right)^{-2} \\
&\times \left(\frac{\nu}{1.4 \text{ GHz}}\right)^{-1} (1 + \bar{r}^2)^{-3\beta+1/2} (1 + z)^{-4} \text{ mJy arcmin}^{-2}.
\end{aligned} \tag{A13}$$

Using the correlations eq. (6), we have

$$\nu L_{\nu}^{\text{sync},e^{\pm}} \simeq 3.0 \cdot 10^{40} \frac{B^2}{B_{\text{CMB}}^2 + B^2} \beta_{\text{core},-4} T_1^{3.06} (1 + z)^{-4} \text{ erg s}^{-1} \tag{A14}$$

and

$$\begin{aligned}
S_{\nu}^{\text{sync},e^{\pm}}(\bar{r}) &\simeq 9.8 \left(3\beta - \frac{3}{2}\right) \frac{B^2}{B_{\text{CMB}}^2 + B^2} \beta_{\text{core},-4} T_1^{0.42} \\
&\times \left(\frac{\nu}{1.4 \text{ GHz}}\right)^{-1} (1 + \bar{r}^2)^{-3\beta+1/2} (1 + z)^{-4} \text{ mJy arcmin}^{-2}.
\end{aligned} \tag{A15}$$

Primary electrons IC emission

As in the case of the charged secondaries, we assume that the distribution of the primaries is in a steady state, since electrons (at the relevant energies) lose all their energy to radiation on a time scale short compared to the cluster dynamical time, $t_{\text{dyn}} \sim 1 \text{ Gyr}$. Unlike the secondary electrons and positrons, which lose energy through both IC and synchrotron emission, primary electrons lose their energy mainly by IC scattering of CMB photons, since the magnetic field at the accretion shock is expected to be weak, $\sim 0.1 \mu\text{G} \ll B_{\text{CMB}}$ (Waxman & Loeb 2000). Thus the steady state assumption holds for primaries with Lorentz factors $\gamma > \gamma_{\text{cool}} \sim 2000$.

To a very good approximation, in the range of photon energies $\gamma_{\text{cool}}^2 3T_{\text{CMB}}(1+z)^4 < \varepsilon_{\text{ph}} < \gamma_{\text{max}}^2 3T_{\text{CMB}}(1+z)^4$, the luminosity of IC emission by primary, shock accelerated, electrons is given by

$$\begin{aligned}
\nu L_{\nu}^{\text{IC,shock}} &\simeq \frac{1}{2} \frac{3}{2} \frac{\eta_e f_b (\mu m_p)^{-1} T}{\ln(p_{\text{max}}) - \ln(m_e c)} f_{\text{inst}} \frac{M_{200}}{t_H} \\
&\simeq 1.8 \cdot 10^{43} (f_{\text{inst}} \eta_e)_{-2} \beta^{3/2} \left(\frac{f_b}{0.17}\right) T_1^{5/2} \bar{Z}(z) \text{ erg s}^{-1},
\end{aligned} \tag{A16}$$

where $(f_{\text{inst}} \eta_e)_{-2} \simeq f_{\text{inst}} \eta_e / 10^{-2}$, $f_b = \Omega_b / \Omega_m$ and $\bar{Z}(z) \equiv (t_H H(z))^{-1}$. Assuming that the primary electron emission originates from a thin layer of thickness w behind the accretion shock, the IC surface brightness is given by

$$\begin{aligned}
S_{\nu > \nu_{\text{min}}}^{\text{IC,shock}}(r) &\simeq \frac{1}{8\pi^2 r_{200}^2} \xi(r/r_{200}, w/r_{200}) \nu L_{\nu}^{\text{IC,shock}} (\varepsilon_{\nu, \text{min}})^{-1} \\
&\simeq 1.5 \cdot 10^{-7} (f_{\text{inst}} \eta_e)_{-2} \beta^{1/2} \left(\frac{f_b}{0.17}\right) T_1^{3/2} \\
&\times \left(\frac{\varepsilon_{\nu, \text{min}}}{10 \text{ GeV}}\right)^{-1} \xi(r/r_{200}, w/r_{200}) \\
&\times \bar{Z}(z) h_{70}^2(z) \text{ ph cm}^{-2} \text{ s}^{-1} \text{ sr}^{-1},
\end{aligned} \tag{A17}$$

where

$$\xi(x, y) = \begin{cases} \frac{3(\sqrt{1-x^2} - \sqrt{(1-y)^2 - x^2})}{1 - (1-y)^3}, & x \leq 1 - y \\ \frac{3\sqrt{1-x^2}}{1 - (1-y)^3}, & 1 - y < x < 1 \end{cases}. \tag{A18}$$

For $w \ll r_{200}$, $\xi(x, y)$ can be approximated in the regime $x < 1 - y$ as

$$\xi(x, y) \simeq \frac{1}{\sqrt{1-x^2}}. \tag{A19}$$

The thickness of the emitting region is approximately given by the product of the cooling time of the emitting electrons and the velocity of the downstream fluid relative to the shock velocity. As explained in § 2, the approximation $w \ll r_{200}$ holds for $\gamma > \gamma_{\text{cool}} \sim 2000$.

Primary electrons synchrotron emission

The synchrotron luminosity from these electrons in the range of photon energies $\gamma_{\text{cool}}^2 \varepsilon_0 < \varepsilon_{\text{ph}} < \gamma_{\text{max}}^2 \varepsilon_0$, is given by

$$\begin{aligned} \nu L_{\nu}^{\text{sync,shock}} &\simeq \nu L_{\nu}^{\text{IC,shock}} \frac{B^2}{B_{\text{CMB}}^2} \\ &\simeq 1.7 \cdot 10^{40} (f_{\text{inst}} \eta_e)_{-2} \beta^{3/2} \left(\frac{f_b}{0.17} \right) T_1^{5/2} B_{-7}^2 \bar{Z}(z) (1+z)^{-4} \text{erg s}^{-1}, \end{aligned} \quad (\text{A20})$$

where $B_{-7} = B/0.1 \mu\text{G}$. The synchrotron surface brightness from the shock is

$$\begin{aligned} S_{\nu}^{\text{sync,shock}}(r) &\simeq \frac{1}{8\pi^2 r_{200}^2} \xi(r/r_{200}, w/r_{200}) \nu L_{\nu}^{\text{sync,shock}}(\nu)^{-1} \\ &\simeq 1.4 \cdot 10^{-2} (f_{\text{inst}} \eta_e)_{-2} \beta^{1/2} \left(\frac{f_b}{0.17} \right) T_1^{3/2} B_{-7}^2 \left(\frac{\nu}{1.4 \text{GHz}} \right)^{-1} \\ &\times \xi(r/r_{200}, w/r_{200}) \bar{Z}(z) h_{70}^2(z) (1+z)^{-4} \text{mJy arcmin}^{-2}. \end{aligned} \quad (\text{A21})$$

B. PRESS-SCHECHTER ACCRETION RATE

In the Press-Schechter formalism, it is convenient to use $\omega \equiv \delta_c(z) = \delta_{c,0}/D(z)$ as the time variable (where $\delta_{c,0}$ is the density contrast estimated by linear theory for the virialization of a spherical halo, and $D(z)$ is the linear growth factor), and $S(M) \equiv \sigma^2(M)$, the mass variance, as the mass variable. The probability for a step ΔS in a time-step $\Delta\omega$ is

$$P(\Delta S, \Delta\omega) d\Delta S = \frac{1}{\sqrt{2\pi}} \frac{\Delta\omega}{(\Delta S)^{3/2}} \exp\left[-\frac{(\Delta\omega)^2}{2\Delta S}\right] d\Delta S. \quad (\text{B1})$$

Changing variables, $x \equiv \Delta\omega/(2\sqrt{\Delta S})$, this becomes a Gaussian distribution in x with zero mean and unit variance. Since $\Delta S \propto \Delta\omega^2$, the accretion rate, $\Delta S/\Delta\omega$, is linear in $\Delta\omega$ and thus tends to zero as $\Delta\omega \rightarrow 0$.

In order to obtain a finite mass accretion rate in our scheme, we introduce a slight correction to the treatment of masses below the mass resolution, M_l : Each time a mass step ΔM is drawn, which is below the mass resolution M_l , we assume that mass was accreted during $\Delta\omega$ at a constant rate, $(dM/d\omega)_{M_l, \text{acc}}$, which is the average accretion rate below M_l . Let us next calculate $(dM/d\omega)_{M_l, \text{acc}}$. The average mass of the progenitors of some mass M_0 that contributed to M_0 through accretion over a time step $\Delta\omega$ is

$$\bar{M}_{\text{acc}, \Delta\omega} = \int_{M_0 - M_l}^{M_0} P(M|M_0, \Delta\omega) M dM = M_0 \left[1 - \text{erf}\left(\frac{\Delta\omega}{\sqrt{2S(M_l) - 2S(M_0)}}\right) \right]. \quad (\text{B2})$$

Since

$$\frac{\bar{M}_{\text{acc}, \Delta\omega} - M_0}{\Delta\omega} \xrightarrow{\Delta\omega \rightarrow 0} -\sqrt{\frac{2}{\pi}} \frac{M_0}{\sqrt{S(M_l) - S(M_0)}}, \quad (\text{B3})$$

we have

$$\left(\frac{dM}{d\omega} \right)_{M_l, \text{acc}} = -\sqrt{\frac{2}{\pi}} \frac{M_0}{\sqrt{S(M_l) - S(M_0)}}. \quad (\text{B4})$$

REFERENCES

- Araudo, A. T., Cora, S. A., & Romero, G. E. 2008, MNRAS, 390, 323, 0807.3497
 Arnaud, M., & Evrard, A. E. 1999, MNRAS, 305, 631, arXiv:astro-ph/9806353
 Balogh, M. L., Babul, A., & Patton, D. R. 1999, MNRAS, 307, 463, arXiv:astro-ph/9809159
 Balogh, M. L., Pearce, F. R., Bower, R. G., & Kay, S. T. 2001, MNRAS, 326, 1228, arXiv:astro-ph/0104041
 Berezhinsky, V., Blasi, P., & Ptuskin, V. 1997, ApJ, 487, 529
 Berrington, R., & Dermer, C. 2003, ApJ, 594, 709
 Blandford, R., & Eichler, D. 1987, Phys. Rep., 154, 1
 Blasi, P., & Colafrancesco, S. 1999, Astroparticle Physics, 12, 169, arXiv:astro-ph/9905122
 Blumenthal, G., & Gould, R. 1970, Rev. Mod. Phys., 42, 237
 Borgani, S. et al. 2006, MNRAS, 367, 1641, arXiv:astro-ph/0512506
 ——. 2004, MNRAS, 348, 1078, arXiv:astro-ph/0310794
 Brunetti, G., & Blasi, P. 2005, MNRAS, 363, 1173, arXiv:astro-ph/0508100
 Brunetti, G., Blasi, P., Cassano, R., & Gabici, S. 2004, MNRAS, 350, 1174, arXiv:astro-ph/0312482
 Brunetti, G., Blasi, P., Cassano, R., & Gabici, S. 2008, in American Institute of Physics Conference Series, Vol. 1085, American Institute of Physics Conference Series, 628–631
 Brunetti, G., Setti, G., Feretti, L., & Giovannini, G. 2001, MNRAS, 320, 365, arXiv:astro-ph/0008518
 Bykov, A. M., Bloemen, H., & Uvarov, Y. A. 2000, A&A, 362, 886
 Cassano, R., & Brunetti, G. 2005, MNRAS, 357, 1313, arXiv:astro-ph/0412475
 Cassano, R., Brunetti, G., Setti, G., Govoni, F., & Dolag, K. 2007, MNRAS, 378, 1565, 0704.3490
 Cavaliere, A., & Fusco-Femiano, R. 1976, A&A, 49, 137
 Cavaliere, A., Menci, N., & Tozzi, P. 1997, ApJ, 484, L21+, arXiv:astro-ph/9705058
 Colafrancesco, S., & Blasi, P. 1998, Astroparticle Physics, 9, 227, arXiv:astro-ph/9804262
 Dar, A., & Shaviv, N. J. 1995, Physical Review Letters, 75, 3052, arXiv:astro-ph/9501079
 de Plaa, J. et al. 2006, A&A, 452, 397, arXiv:astro-ph/0602582
 Dennison, B. 1980, ApJ, 239, L93
 Domainko, W., Benbow, W., Hinton, J., Martineau-Huynh, O., de Naurio, M., Nedbal, D., Pedalletti, G., & Rowell, G. 2007, Arxiv preprint arXiv:0708.1384

- Eckert, D., Neronov, A., Courvoisier, T., & Produit, N. 2007, *A&A*, 470, 835
- Eke, V., Navarro, J., & Steinmetz, M. 2001, *ApJ*, 554, 114
- Enßlin, T. A. 2002, *A&A*, 396, L17, arXiv:astro-ph/0211017
- Enßlin, T. A., Pfrommer, C., Springel, V., & Jubelgas, M. 2007, *A&A*, 473, 41, arXiv:astro-ph/0603484
- Evrard, A. E., & Henry, J. P. 1991, *ApJ*, 383, 95
- Fabian, A. C. 1994, *ARA&A*, 32, 277
- Fabian, A. C., Pringle, J. E., & Rees, M. J. 1976, *Nature*, 263, 301
- Feretti, L. 2005, *Advances in Space Research*, 36, 729
- Franceschini, A., Rodighiero, G., & Vaccari, M. 2008, *A&A*, 487, 837
- Fujita, Y., Kohri, K., Yamazaki, R., & Kino, M. 2007, *ApJ*, 663, L61, 0705.4284
- Fujita, Y., & Sarazin, C. 2001, *ApJ*, 563, 660
- Fujita, Y., Takizawa, M., & Sarazin, C. L. 2003, *ApJ*, 584, 190, arXiv:astro-ph/0210320
- Fusco-Femiano, R., Dal Fiume, D., Feretti, L., Giovannini, G., Grandi, P., Matt, G., Molendi, S., & Santangelo, A. 1999, *ApJ*, 513, L21
- Fusco-Femiano, R., Landi, R., & Orlandini, M. 2007, *ApJ*, 654, L9, arXiv:astro-ph/0611325
- Fusco-Femiano, R., Orlandini, M., Brunetti, G., Feretti, L., Giovannini, G., Grandi, P., & Setti, G. 2004, *ApJ*, 602, L73
- Gabici, S., & Blasi, P. 2003, *ApJ*, 583, 695
- Gorenstein, P., Fabricant, D., Topka, K., Harnden, Jr., F. R., & Tucker, W. H. 1978, *ApJ*, 224, 718
- Inoue, S., Aharonian, F. A., & Sugiyama, N. 2005, *ApJ*, 628, L9, arXiv:astro-ph/0505398
- Jones, C., & Forman, W. 1984, *ApJ*, 276, 38
- Jubelgas, M., Springel, V., Enßlin, T., & Pfrommer, C. 2008, *A&A*, 481, 33, arXiv:astro-ph/0603485
- Kaiser, N. 1991, *ApJ*, 383, 104
- Kamae, T., Karlsson, N., Mizuno, T., Abe, T., & Koi, T. 2006, *ApJ*, 647, 692
- Katz, B., & Waxman, E. 2008, *Journal of Cosmology and Astro-Particle Physics*, 1, 18, 0706.3485
- Katz, J. I. 1976, *ApJ*, 207, 25
- Kawasaki, W., & Totani, T. 2002, *ApJ*, 576, 679, arXiv:astro-ph/0108309
- Keshet, U., Waxman, E., Loeb, A., Springel, V., & Hernquist, L. 2003, *ApJ*, 585, 128
- Kravtsov, A. V., Nagai, D., & Vikhlinin, A. A. 2005, *ApJ*, 625, 588, arXiv:astro-ph/0501227
- Kushnir, D., Katz, B., & Waxman, E. 2009, *Journal of Cosmology and Astro-Particle Physics*, 9, 24, 0903.2275
- Kushnir, D., & Waxman, E. 2010, *Journal of Cosmology and Astro-Particle Physics*, 2, 25, 0905.1950
- Lacey, C., & Cole, S. 1993, *MNRAS*, 262, 627
- Loeb, A., & Waxman, E. 2000, *Nature*, 405, 156
- Lutovinov, A. A., Vikhlinin, A., Churazov, E. M., Revnivtsev, M. G., & Sunyaev, R. A. 2008, *ApJ*, 687, 968, 0802.3742
- Markevitch, M. 1998, *ApJ*, 504, 27, arXiv:astro-ph/9802059
- McCarthy, I. et al. 2007, *MNRAS*, 376, 497
- Miniati, F. 2003, *MNRAS*, 342, 1009
- Molnar, S. M., Hearn, N., Haiman, Z., Bryan, G., Evrard, A. E., & Lake, G. 2009, ArXiv e-prints, 0902.3323
- Murase, K., Inoue, S., & Nagataki, S. 2008, *ApJ*, 689, L105, 0805.0104
- Navarro, J., Frenk, C., & White, S. 1997, *ApJ*, 490, 493
- Navarro, J. F., Frenk, C. S., & White, S. D. M. 1995, *MNRAS*, 275, 720, arXiv:astro-ph/9408069
- Perkins, J. et al. 2006, *ApJ*, 644, 148
- Perkins, J. S. 2008, in *American Institute of Physics Conference Series*, Vol. 1085, American Institute of Physics Conference Series, 569–572
- Petrosian, V. 2001, *ApJ*, 557, 560, arXiv:astro-ph/0101145
- Pfrommer, C. 2008, *MNRAS*, 385, 1242
- Pfrommer, C., Enßlin, T., & Springel, V. 2008, *MNRAS*, 385, 1211
- Pfrommer, C., Enßlin, T., Springel, V., Jubelgas, M., & Dolag, K. 2007, *MNRAS*, 378, 385
- Pfrommer, C., Springel, V., Enßlin, T. A., & Jubelgas, M. 2006, *MNRAS*, 367, 113, arXiv:astro-ph/0603483
- Ponman, T. J., Cannon, D. B., & Navarro, J. F. 1999, *Nature*, 397, 135, arXiv:astro-ph/9810359
- Press, W., & Schechter, P. 1974, *ApJ*, 187, 425
- Reimer, O., Pohl, M., Sreekumar, P., & Mattox, J. 2003, *ApJ*, 588, 155
- Reiprich, T., & Bohringer, H. 2002, *ApJ*, 567, 716
- Rephaeli, Y., & Gruber, D. 2002, *ApJ*, 579, 587
- Rephaeli, Y., Gruber, D., & Blanco, P. 1999, *ApJ*, 511, 21
- Rephaeli, Y., Nevalainen, J., Ohashi, T., & Bykov, A. M. 2008, *Space Science Reviews*, 134, 71, 0801.0982
- Roncarelli, M., Ettori, S., Dolag, K., Moscardini, L., Borgani, S., & Murante, G. 2006, *MNRAS*, 373, 1339, arXiv:astro-ph/0609824
- Ryu, D., Kang, H., Hallman, E., & Jones, T. 2003, *ApJ*, 593, 599
- Sarazin, C. 1999, *ApJ*, 520, 529
- Sarazin, C. L., & Bahcall, J. N. 1977, *ApJS*, 34, 451
- Scharf, C. A., & Mukherjee, R. 2002, *ApJ*, 580, 154, arXiv:astro-ph/0207411
- Skillman, S. W., O’Shea, B. W., Hallman, E. J., Burns, J. O., & Norman, M. L. 2008, *ApJ*, 689, 1063, 0806.1522
- Thierbach, M., Klein, U., & Wielebinski, R. 2003, *A&AS*, 397, 53
- Totani, T., & Kitayama, T. 2000, *ApJ*, 545, 572, arXiv:astro-ph/0006176
- Vikhlinin, A., Kravtsov, A., Forman, W., Jones, C., Markevitch, M., Murray, S., & Van Speybroeck, L. 2006, *ApJ*, 640, 691
- Vikhlinin, A., Markevitch, M., Murray, S. S., Jones, C., Forman, W., & Van Speybroeck, L. 2005, *ApJ*, 628, 655, arXiv:astro-ph/0412306
- Voigt, L. M., & Fabian, A. C. 2004, *MNRAS*, 347, 1130, arXiv:astro-ph/0308352
- Voit, G., Bryan, G., Balogh, M., & Bower, R. 2002, *ApJ*, 576, 601
- Völk, H., Aharonian, F., & Breitschwerdt, D. 1996, *Space Sci. Rev.*, 75, 279
- Waxman, E., & Loeb, A. 2000, *ApJ*, 545, L11, arXiv:astro-ph/0007049